Summer 8-8-2015

Crystal Structure, Electronic Structure, and Physicochemical Characterization of I2-II-IV-VI4 and I4-II-IV2-VI7 Diamond-Like Semiconductors Prepared by High-Temperature Solid-State Synthesis

Charles Sinagra

Recommended Citation

Sinagra, C. (2015). Crystal Structure, Electronic Structure, and Physicochemical Characterization of I2-II-IV-VI4 and I4-II-IV2-VI7 Diamond-Like Semiconductors Prepared by High-Temperature Solid-State Synthesis (Master's thesis, Duquesne University). Retrieved from https://dsc.duq.edu/etd/1510

CRYSTAL STRUCTURE, ELECTRONIC STRUCTURE, AND PHYSICOCHEMICAL CHARACTERIZATION OF I_2-II-IV-VI_4 and I_4-II-IV_2-VI_7 DIAMOND-LIKE SEMICONDUCTORS PREPARED BY HIGH-TEMPERATURE SOLID-STATE SYNTHESIS

A Thesis

Submitted to the Bayer School

of Natural and Environmental Sciences

Duquesne University

In partial fulfillment of the requirements for

the degree of Masters of Chemistry

By

Charles W. Sinagra III

August 2015

CRYSTAL STRUCTURE, ELECTRONIC STRUCTURE, AND PHYSICOCHEMICAL CHARACTERIZATION OF I_2-II-IV-VI_4 and I_4-II-IV_2-VI_7 DIAMOND-LIKE SEMICONDUCTORS PREPARED BY HIGH-TEMPERATURE SOLID-STATE SYNTHESIS

By

Charles W. Sinagra III

Approved July 8, 2015

Jennifer A. Aitken, Ph.D. Associate Professor of Chemistry (Committee Chair)	Tomislav Pintauer, Ph.D. Associate Professor of Chemistry (Committee Member)
Stephanie J. Wetzel, Ph.D. Assistant Professor of Chemistry (Committee Member)	Charles H. Lake, Ph.D. Professor of Chemistry (Outside Reader)
Philip Reeder, Ph.D. Dean and Professor, Bayer School of Natural and Environmental Sciences	Ralph A. Wheeler, Ph.D. Chair, Department of Chemistry Professor of Chemistry

ABSTRACT

CRYSTAL STRUCTURE, ELECTRONIC STRUCTURE, AND PHYSICOCHEMICAL CHARACTERIZATION OF I_2-II-IV-VI_4 and I_4-II-IV_2-VI_7 DIAMOND-LIKE SEMICONDUCTORS PREPARED BY HIGH-TEMPERATURE SOLID-STATE SYNTHESIS

By

Charles W. Sinagra III

August 2015

Thesis supervised by Dr. Jennifer A. Aitken

Diamond-like semiconductors are compounds that possess bandgaps in the visible to near-infrared and crystallize in structures derived from that of cubic or hexagonal diamond. The compositions of quaternary DLSs are predictable and flexible, which allows for the tuning of physicochemical properties for technological applications. Chapter 1 provides an overview of DLSs and potential applications for which they are useful. In this work, diamond-like semiconductors (DLSs) of the family I_2-II-IV-VI_4, namely, $Cu_2ZnGeSe_4$ and $Cu_2MnGeSe_4$, were prepared via high-temperature solid-state synthesis Investigations to prepare $Cu_2ZnGeSe_4$, led to the serendipitous discovery of a new compound, $Cu_4ZnGe_2Se_7$. To better understand the relationships between these

compounds and their potential for applications, crystal structure, electronic structure, and physicochemical characterization were performed. Chapter 2 details the synthesis and characterization techniques implemented for these compounds.

Chapter 3 describes the relationships between these I_2-II-IV-VI_4 and I_4-II-IV_2-VI_7 compounds, specifically $Cu_2ZnGeSe_4$ and the $Cu_4ZnGe_2Se_7$, along with the differences in the resulting physicochemical properties. Single crystal X-ray diffraction was used to solve and refine the structure of $Cu_4ZnGe_2Se_7$, which was found to crystallize in the monoclinic *C*2 space group. Rietveld refinement of synchrotron X-ray powder diffraction (XRPD) data for $Cu_4ZnGe_2Se_7$ confirmed the structure and indicated ~ 95 wt. % phase purity with ~ 5 wt. % of $Cu_2ZnGeSe_4$ present as a secondary phase. Rietveld refinement of synchrotron XRPD data for $Cu_2ZnGeSe_4$ confirmed the previously reported stannite structure in space group *I*-42*m*. $Cu_2ZnGeSe_4$ and $Cu_4ZnGe_2Se_7$ both were found to be direct-gap semiconductors by optical diffuse reflectance spectroscopy, with bandgap values of 1.38 eV and 0.91 eV, respectively.

The discovery of the new compound, $Cu_4ZnGe_2Se_7$, prompted further research into the family of materials having the formula I_4-II-IV_2-VI_7, specifically Cu_4-II-Ge_2-Se_7 where II = Mn, Fe, Co, and Ni. This investigation was successful by leading into the discovery of more new I_4-II-IV_2-VI_7 phases as described in the Appendix. Due to relatively lower bandgaps, a more distorted diamond-like structure, and a chemical formula naturally containing more copper, these compounds may be even better candidates for thermoelectric applications.

ACKNOWLEDGEMENT

I would first like to thank my wonderful advisor, Dr. Jennifer Aiken, who has led me along this journey and has always pushed me in the right direction. Her leadership and dedication really helped me complete this goal and I don’t think I would be where I am now if it wasn’t for her motivation. Working with Dr. Aitken was the perfect combination of a challenging yet comfortable atmosphere, where hard work was expected, but questions were welcomed. All in all, Dr. Aitken is not only a brilliant advisor, but she is an amazing person, and it was a privilege to work for her. I would also like to thank my committee members, Dr. Tomislav Pintauer, Dr. Stephanie Wetzel, and Dr. Charles Lake for their continued support.

I also owe a lot of gratitude to the Aitken Team, especially recent graduates Dr. Kimberly Rosmus and Dr. Jacilynn Brant, who taught me so much about the lab and who were always there to help me along the way. Having these two senior students in the lab provided great role models and a wealth of knowledge for me to learn from. They both had a hand in teaching me how to use all of the instruments necessary for the characterization techniques we perform in our lab. I would also like to specifically thank my buddy Dr. Jian-Han Zhang who was the post-doc in our lab. He was definitely my best resource in the lab, but he was also my best friend throughout my graduate studies and I’m sure we will be friends for life. He also performed the electronic structure calculations for my compounds using the total-energy code of CASTEP.

Thank you to Duquesne University, specifically the Bayer School of Natural and Environmental Sciences for allowing me to conduct my research here. Also, a great thank you to the National Science Foundation (DMR-0645304 and DMR-1201729) for funding to make this work possible. I would like to thank the U.S. Department of Energy, Office of Science, Office of Basic Energy Science, under contract DE-AC02-06CH11357 for the use of the Advanced Photon Source at Argonne National Laboratory for the collection of synchrotron X-ray powder diffraction data. Instrumentation was purchased through National Science Foundation grants; DUE-0511444 for the Panalytical X'Pert Pro diffractometer, CRIF-0234872 for the Bruker Apex 2 diffractometer, and MRI-CHE-0923183 for the Hitachi S3400N scanning electron microscope. I would also like to thank RJ Lee Group Inc. in Monroeville, PA for performing inductively coupled plasma optical emission spectroscopy on my compounds. Although not presented in this thesis, I would like to thank Dr. Joon Jang and his group as well as Dr. Sabah Bux for work they are continuing to do on my samples that should be eventually published.

Finally, I would like to thank my family for the support and encouragement throughout this process. I would like to especially thank my mom, Joyce Sinagra, who has always pushed me to be the best I can be. I would also like to thank my beautiful wife, Brittany Sinagra, for my being my rock throughout all the ups and downs. The little notes of encouragement you left on my laptop of the mornings of a big presentation meant more then you know. I dedicate this thesis to my son, Charles W. Sinagra IV. All this hard work is for you baby boy, so that I can give you the life you deserve.

TABLE OF CONTENTS

Page

LIST OF TABLES

LIST OF FIGURES

1. An Introduction to Diamond-like Semiconductors

1.1 Introduction

Diamond-like semiconductors (DLSs) have recently seen an increase in attention due to their useful applications in photovoltaics,[1-4] nonlinear optics (NLO),[5,6] and thermoelectrics.[7-9] In particular, this research will focus on compounds with potential applications in nonlinear optics and thermoelectrics. There is specific interest in I_2-II-IV-VI_4 quaternary DLSs in comparison to binary and ternary DLSs due to their flexible composition and the ability to optimize their properties.[10-12] Furthermore, this compositional flexibility can allow for systematic studies of structure-property and composition-property relationships in these materials. Solid solutions of these compounds can also be explored to further fine tune properties to make them more attractive for technological applications.[13-16] The current generation of photovoltaic materials is based on the ternary $CuInSe_2$ DLS; however, new materials are sought after for higher efficiencies and because indium is becoming more rare and thus expensive.[17] Quaternary DLSs, such as $Cu_2ZnSnSe_4$, are already potential candidates for the next generation of solar cells due to their optimal bandgaps of around 1.5 eV[18] and their properties that may be further optimized by compositional tuning.[19,20] Ternary DLSs, such as $AgGaS_2$ and $AgGaSe_2$ are presently commercially available for second harmonic generation (SHG) applications and are considered the benchmark NLO materials for use in the infrared.[21,22] However, both of these compounds contain an increasingly non-abundant element, gallium, and have relatively low laser damage thresholds (LDTs) limiting their use in high-powered laser applications.[21] Quaternary materials of the I_2-II-IV-VI_4 variety have been previously synthesized in the Aitken lab and have produced significant SHG responses along with some of the most impressive LDTs to date.[23,24] This family of I_2-II-IV-VI_4 DLSs may also find use in thermoelectric applications, such as harnessing waste heat for the production of electricity. For example, $Cu_{2.1}Zn_{0.9}SnSe_4$ has demonstrated a thermoelectric figure of merit (ZT) of 0.91 at 850K.[25] Because materials with increased ZT are sought after for thermoelectric applications, discovery of new DLSs and optimization of existing DLSs are warranted. Due to these promising results, the initial goal of this work was to synthesize and characterize two I_2-II-IV-VI_4 diamond-like semiconductors, $Cu_2ZnGeSe_4$ and $Cu_2MnGeSe_4$. Even though both of these compounds have been previously reported in the literature, there are limited data available regarding the optical and thermoelectric properties for these materials. Furthermore, the idea of substitution and solid-solutions (i.e. $Cu_{2.1}Zn_{0.9-x}Mn_xGeSe_4$) could also be explored to fine-tune the properties of these materials. Although previously prepared by others, literature accounts of synthetic procedures are often not entirely reproducible from lab-to-lab; therefore, the first step in this work was to prepare the two compounds, $Cu_2ZnGeSe_4$ and $Cu_2MnGeSe_4$, as phase-pure materials. Investigations to prepare these I_2-II-IV-VI_4 compounds, specifically $Cu_2ZnGeSe_4$, led to the serendipitous discovery of a new compound, $Cu_4ZnGe_2Se_7$. This prompted further exploration into this family of materials having the general formula I_4-II-IV_2-VI_7, specifically Cu_4-II-Ge_2-Se_7 where II = Mn, Fe, Co, and Ni. This investigation was successful, leading to the discovery of more new I_4-II-IV_2-VI_7 phases. Due to relatively lower bandgaps, a more distorted diamond-like structure, and a chemical formula naturally containing more copper, this new I_4-II-IV_2-VI_7 family may be even better candidates for thermoelectric applications. This work describes the relationships between the $Cu_2ZnGeSe_4$ and the

$Cu_4ZnGe_2Se_7$ structures, along with the differences in the resulting physicochemical properties.

1.2 Fundamentals of Diamond-Like Semiconductors

There are three types of solids: metals, semiconductors, and insulators. Each is defined by their electrical properties. The ability to conduct electricity directly correlates with the electronic band structure of a material. In conductors, for example pure metals, the filled and empty bands overlap, so that electrons can easily move within the bands to conduct electricity. In a semiconductor, the bandgap energy, which is the energy needed to promote the flow of electrons, is defined as the energy between the top of the filled valence band and bottom of the empty conduction band. Insulators, for example plastic, rubber, or diamond, are poor conductors of electricity and have a large bandgap, greater than 3.5 eV. Thus, electrons cannot easily gain enough energy to move from the valence band to the conduction band to easily allow for conduction. Semiconductors, for example silicon, have bandgaps that are much smaller than those of insulators; therefore, less energy is necessary to promote an electron from the valence band to the conduction band. Semiconductors are very important in the electronics industry and their bandgaps can be optimized for specific applications by doping or chemical substitutions. Diamond-like semiconductors are made from a variety of elements, have a number of possible formulae, possess bandgaps between zero and ~3.5 eV and maintain a structure that can be considered as a derivative of diamond.[26]

For a compound to possess a diamond-like structure there are four guidelines that need to be followed.[27] The first guideline is that the average number of valence electrons must equal four, which is the same number of valence electrons in carbon (the element that makes up diamond).[27] For example, $Cu_2ZnGeSe_4$ has 2 copper atoms, each with 1 valence electron, 1 zinc atom with 2 valence electrons, 1 germanium atom with 4 valence electrons, and 4 selenium atoms with 6 valence electrons. When all atoms are taken into account, there are a total of 32 valence electrons in one formula unit. This number of electrons is then divided by the number of atoms in the formula (8) resulting in an average of 4 valence electrons per atom. Equation 1.1 can be used as a general formula to determine the average number of valence electrons in a diamond-like semiconductor.

$$VE_{avg} = ((ve_c+ve_a)/(n_c+n_a)) \quad \text{(Eq. 1.1)}$$

The total number of valence electrons of the cations in the formula unit is represented by ve_c and the total number of valence electrons of the anions in the formula unit is shown as ve_a. These numbers are summed and then divided by the sum of the total number of cations (n_c) and anions (n_a) in the formula unit, to determine the average number of valence electrons (VE_{avg}).

The second guideline is that the number of valence electrons per anion must equal eight.[27] Again using $Cu_2ZnGeSe_4$ as an example, dividing the 32 electrons by its 4 anions results in 8 electrons per anion. The average number of valence electrons per anion can be calculated by using Equation 1.2.

$$VE_a = ((ve_c+ve_a)/n_a) \quad \text{(Eq. 1.2)}$$

Again, the total number of valence electrons in the formula unit is determined by summing the total number of valence electrons of the cations (ve_c) and anions (ve_a). This number is then divided by the total number of anions in the formula unit (n_a) to determine the average number of valence electrons per anion (VE_a).

The third guideline is that all ions must be tetrahedrally coordinated.[26] Pauling's first rule, the radius ratio rule, can be used as a guide. Linus Pauling was very interested in the bonding between atoms which led him to study crystallography and crystal structures.[28] After years of research in this field, he created a list of rules to explain the trends in the known crystal structures at that time, as well as to help determine new crystal structures.[29] His first rule states that the radius of the cation divided by that of the anion should be of some minimal critical value in order for a certain coordination polyhedron to exist.[29] According to Pauling's paper, a radius ratio in the range of 0.25-0.414 predicts a coordination number of four. However, previous work has reported that the radius ratios between ions in many diamond-like compounds, which exhibit tetrahedral coordination, do not always fall within that range.[30] This can be explained by the limited known crystal structures Pauling used at the time when he formulated his rules, and the fact that the structures included primarily oxides and highly ionic compounds. Selenides are much softer ions and are known to be more iono-covalent in their bonding with metal cations. Nevertheless, the carbon atoms within diamond are all tetrahedrally coordinated; therefore, diamond-like structures must have all ions in a tetrahedral coordination as well.

The fourth and final guideline is Pauling's second rule, the electrostatic valence sum rule, which states that the charge of an anion should be compensated by the cations in its first coordination sphere.[29] This can be proven by determining the strength of the electrostatic valence bond(s), as shown in Equation 1.3:

$$s = z/v, \qquad \text{(Eq. 1.3)}$$

where z is the electric charge of a cation, and v is the coordination number of the cation. To calculate the charge surrounding the anion (ζ), the equation becomes:

$$\zeta = \Sigma_i (z_i/v_i) = \Sigma_i s_i. \quad \text{(Eq. 1.4)}$$

For example, in the compound $Cu_2ZnGeSe_4$, each Se^{2-} ion is surrounded by two Cu^{1+} ions, one Zn^{2+} ion, and one Ge^{4+} ion, where each Cu^{1+} gives s = ¼, Zn^{2+} gives s = ½, and Ge^{4+} gives s=1, resulting in a ζ of 2. The -2 charge of the selenium is compensated by the +2 charge of the total surrounding cations. This is also shown in Figure 1.1 below.

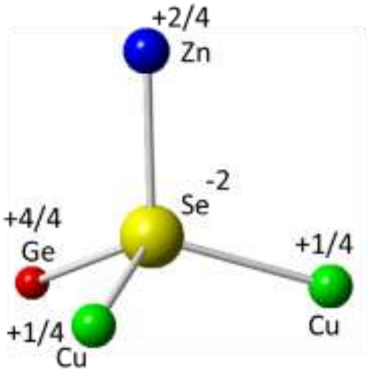

Figure 1.1. Pauling's second rule is satisfied for $Cu_2ZnGeSe_4$. The charge of the selenium atom (-2) is compensated by the first nearest neighbor cations. Each cation contributes its charge divided by 4, since they are each connected to 4 anions. Two copper cations each contribute a +1/4 charge, zinc contributes a +2/4, and germanium contributes a +4/4 charge which totals a +2 charge to compensate the -2 charge of the selenium.

However, strict adherence to Pauling's second rule may not always be required, as even Pauling stated that Eq. 1.4 is not anticipated to satisfy all crystals. This will be discussed later, as the new family of I_4-II-IV_2-VI_7 compounds do not completely follow Pauling's second rule. In the case that the anion is not completely compensated, the differences in the local charges throughout the structure need to be balanced within the crystals through structural distortions.[29] For example, if the absolute value of ζ is less than the absolute value of the charge of the anion, the cations will be more strongly attracted to the anion, thus the bonds will be shortened. However, if the absolute value of ζ is greater than the absolute value of the charge of the anion, then the bonds will be elongated. In either case, a stable compound may still result; yet, the structure will not be perfectly diamond-like, but rather similar to the diamond-like structure with a greater degree of distortions in the tetrahedra.

1.3 Structure

The crystal structure of a DLS can be derived from either the cubic or hexagonal forms of diamond.[26,27] All of the atomic sites in diamond are occupied, of course, by carbon; but, the crystal structures of DLSs are composed of anions and cations, as shown in Figure 1.2. In order to obtain a binary DLS from diamond, one could envision a substitution of half of the carbon atoms for a cation and the other half for an anion. Each cation would need to be coordinated to four anions, as well as each anion being coordinated to four cations. Additional substitutions could be made to produce ternary and quaternary compounds as long as the substitutions allow adherence to the four guidelines for DLSs discussed above. Even though these substitutions are limited by the guidelines, there are a large number of possible compounds to explore and including solid-solutions as well makes the list nearly endless.[31]

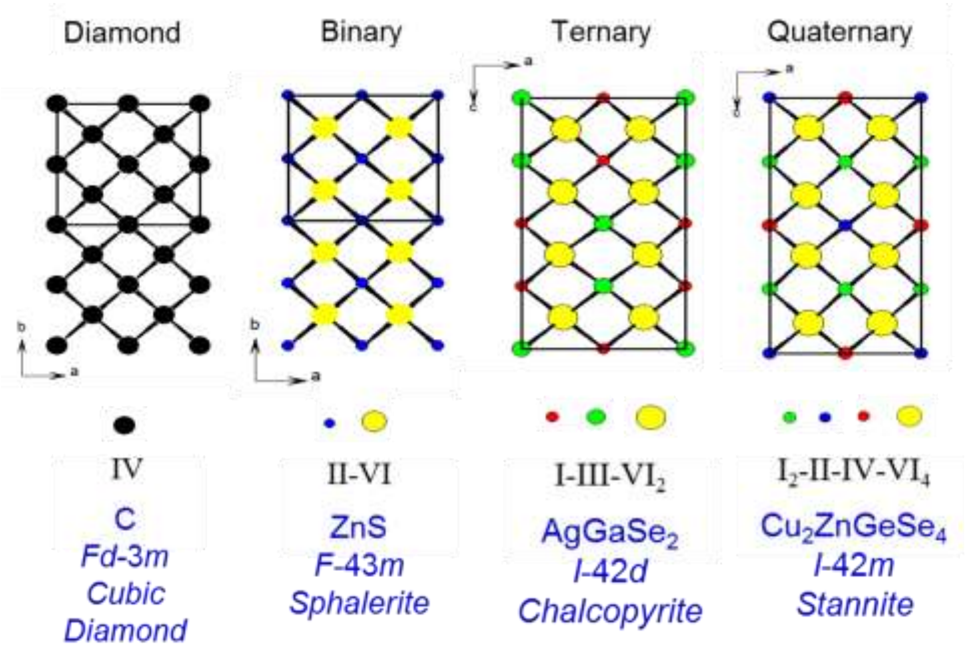

Figure 1.2. Replacing the carbon atoms of cubic diamond with cations and anions results in binary, ternary, and quaternary diamond-like semiconductors, such as ZnS, $AgGaSe_2$, and $Cu_2ZnGeSe_4$, respectively.

1.4 Previous Research

$Cu_2ZnGeSe_4$[32-36] and $Cu_2MnGeSe_4$[32,37] have been previously synthesized and their crystal structures, lattice parameters, and bandgaps have been reported. The I_4-II-IV_2-VI_7 family of compounds that will be discussed in this thesis, specifically Cu_4-II-Ge_2-Se_7 where II = Mn, Fe, Co, Ni, and Zn, is a new set of compounds. However, four compounds of this I_4-II-IV_2-VI_7 formula, namely $Cu_4NiSi_2S_7$,[38] $Cu_4NiGe_2S_7$,[38] $Ag_4HgGe_2S_7$,[39] and $Ag_4CdGe_2S_7$[39] have been previously reported. A summary of these results is below.

1.4.1 I_2-II-IV-VI_4

The lattice parameters of $Cu_2ZnGeSe_4$ and $Cu_2MnGeSe_4$ were first reported by Nitsche et al. in 1967 by using X-ray powder photographs.[32] Single crystals of the materials were synthesized by reacting stoichiometric amounts of the elements in sealed quartz tubes at 1100 °C with the addition of 5 mg iodine/cm^3 and transporting the compounds via the gaseous iodides in a gradient of 800-750 °C.[32] It was reported that the $Cu_2ZnGeSe_4$ crystals had a dark red color with a blade shape and a size of 2 x 0.1 x 0.3 mm.[32] Nitsche used one of these single crystals to solve the structure for $Cu_2ZnGeSe_4$ and reported it to be tetragonal with a sphalerite-like lattice and lattice parameters of a = 5.606 Å and c = 11.024 Å.[32] It was also noted that in comparison to the pattern of stannite, it was probable that $Cu_2ZnGeSe_4$ had the stannite structure with the *I*-42*m* space group.[32] The $Cu_2MnGeSe_4$ crystals were also blades, but they were black and had a size of 8 x 1 x 0.1 mm.[32] Single crystal data was not collected for $Cu_2MnGeSe_4$, but its structure was refined from X-ray powder diffraction patterns and was determined to be orthorhombic with the wurtz-stannite structure-type, crystallizing in the $Pmn2_1$ space group.[32] The reported lattice parameters are a = 7.979 Å, b = 6.865 Å, and c = 6.557 Å.[32] These results were confirmed by Schäfer et al. in 1974, when he also reported that the material had a bandgap of 1.48 eV.[37]

In 1977, Schleich et al. also synthesized $Cu_2ZnGeSe_4$ via iodine transport and reported very similar structural results. They also conducted optical absorption measurements to obtain the bandgap of this material, which was reported to be 1.27 eV.[33] In 2000, $Cu_2ZnGeSe_4$ was again prepared by iodine vapor transport by Lee et al. with a much higher direct bandgap of 1.518 eV.[34] They noted that this discrepancy may be due to the quality of the crystal used for measurements. An enhanced crystal quality was associated with the addition of 5% excess selenium, which was added to all reactions to maintain stoichiometry and to reduce formations of voids in the samples.[34] Lee et al. stated that the crystals used for data collection were closer to correct stoichiometry than the crystals used by Schleich et al.,[33] due to the addition of the excess selenium to compensate for its loss due to the high vapor pressure throughout crystal growth.[34] In this study, $Cu_2ZnGeSe_4$ was again found to have the tetragonal stannite structure, (space group *I*-42*m*) with lattice parameters of a = 5.618 Å and c = 11.040 Å by X-ray powder diffraction.[34] In 2005, Matsushita and Katsui also reported $Cu_2ZnGeSe_4$ to have a tetragonal crystal structure with very similar lattice parameters to those noted previously.[35] In this work, the melting point of $Cu_2ZnGeSe_4$ was determined by differential thermal analysis to be 890 °C.[35] In a more recent study in 2013, Bhaskar et al. again proved the structure of $Cu_2ZnGeSe_4$ and noted a bandgap of 1.63 eV.[36] It was also reported that $Cu_2ZnGeSe_4$ shows p-type semiconductor behavior.[36] Table 1.1 shows the known crystallographic information for both $Cu_2ZnGeSe_4$ and $Cu_2MnGeSe_4$.

Even with all of these previous studies on $Cu_2ZnGeSe_4$ and $Cu_2MnGeSe_4$ there is much physicochemical characterization lacking, specifically nonlinear optical and thermoelectric properties.

Table 1.1. Selected crystallographic information and optical bandgap values for $Cu_2ZnGeSe_4$ and $Cu_2MnGeSe_4$.

	$Cu_2ZnGeSe_4$[32]	**$Cu_2MnGeSe_4$[32]**
Crystal System	Tetragonal	Orthorhombic
Space Group	*I*-42*m*	$Pmn2_1$
Color	Dark Red	Black
Shape	Blades	Blades
Size (mm)	2 x 0.1 x 0.3	8 x 1 x 0.1
a (Å)	5.606	7.979
b (Å)	5.606	6.865
c (Å)	11.024	6.557
E_g (eV)	1.27[33], 1.518[34], 1.63[36]	1.48[37]

1.4.2 I_4-II-IV_2-VI_7

The first I_4-II-IV_2-VI_7 compound was discovered in 1980 when Schäfer et al. reported the crystal structures of $Cu_4NiSi_2S_7$ and $Cu_4NiGe_2S_7$.[38] $Cu_4NiSi_2S_7$ was reported to crystalize in the monoclinic space group *C*2 with a = 11.551 Å, b = 5.313 Å, c = 8.165 Å, β = 98.72 °, and Z = 2.[38] This structure can be considered as a derivative of the cubic diamond-structure. Single crystal photographs of $Cu_4NiGe_2S_7$ showed it to be isotypic with $Cu_4NiSi_2S_7$ having lattice parameters of a = 11.703 Å, b = 5.333 Å, c = 8.311 Å, β = 98.37 °, and Z = 2.[38] In 2002, Gulay et al. discovered two more compounds of the I_4-II-IV_2-VI_7 formula, $Ag_4HgGe_2S_7$ and $Ag_4CdGe_2S_7$.[39] Both compounds crystalize in the monoclinic space group *Cc* with a = 17.454 Å, b = 6.809 Å, c = 10.534 Å, β = 93.398(3) ° and Z = 4 for $Ag_4HgGe_2S_7$ and a = 17.436 Å, b = 6.833 Å, c = 10.535 Å, β = 93.589(3) °, and Z = 4 for $Ag_4CdGe_2S_7$.[39] Table 1.2 summaries the selected crystallographic information for these I_4-II-IV_2-VI_7 compounds. The synthesis and properties of the novel set of compounds Cu_4-II-Ge_2-Se_7, where II = Mn, Fe, Co, Ni, and Zn will be reported in Chapter 3 ($Cu_4ZnGe_2Se_7$) and in the appendix (Cu_4-II-Ge_2-Se_7 where II = Mn, Fe, Co, Ni, and Zn).

Table 1.2. Selected crystallographic information for the known I_4-II-IV_2-VI_7 compounds.

	$Cu_4NiSi_2S_7$[38]	**$Cu_4NiGe_2S_7$**[38]	**$Ag_4HgGe_2S_7$**[39]	**$Ag_4CdGe_2S_7$**[39]
Crystal System	Monoclinic	Monoclinic	Monoclinic	Monoclinic
Space Group	*C*2	*C*2	*Cc*	*Cc*
a (Å)	11.551(2)	11.703(3)	17.454(8)	17.436(8)
b (Å)	5.313(5)	5.333(4)	6.809(2)	6.833(3)
c (Å)	8.165(8)	8.311(2)	10.534(3)	10.535(4)
β (°)	98.72(1)	98.37(1)	93.398(3)	93.589(3)

1.5 Applications of DLSs

1.5.1 Photovoltaics

Solar cells are electrical devices that convert sunlight directly into electricity and can provide an alternative energy source to decrease the amount of carbon-based power.[40,41] Substituted copper indium gallium selenide (CIGS), a I-III-VI_2 DLS with the chalcopyrite structure, is commercially available as the absorber layer in thin film solar cells.[40,42,43] Thus far CIGS solar cells, one of the most commonly used (second to silicon), have reached 21% efficiency in the conversion of solar energy.[12,44] However, CIGS and solid solutions based on this material are synthesized using a substantial amount of indium metal, which is expensive and becoming increasingly rare.[17] It has been estimated that indium could be completely mined out by the year 2068.[44] Therefore, research involving the production of indium-free solar cells using highly abundant and low cost elements is essential. It is also a current goal to find materials with improved efficiencies, so that solar energy could provide a greater portion of the world's energy needs.

Recently, copper-based quaternary chalcogenides have attracted tremendous attention as the most promising low cost alternatives to CIGS solar cells.[43] In particular, the quaternary DLSs Cu_2ZnSnS_4 (CZTS) and $Cu_2ZnSnSe_4$ (CZTSe) are serious contenders for next generation solar cells due to their optimal direct bandgaps around 1.5 eV.[43] Doping of elements, for example Si, into CZTS, has shown the potential to fine tune the absorption edge to the optimum value for solar cell devices in order to achieve high photovoltaic conversion efficiency.[45] Furthermore, Todorov et al. prepared a solar cell device with an impressive 9.6% efficiency using a solid solution based on the two quaternary compounds, Cu_2ZnSnS_4 (CZTS) and $Cu_2ZnSnSe_4$ (CZTSe).[4] These compounds are also attractive due to their earth-abundant elements, low toxicity, and high absorption coefficients.[43,46,47] It has also been reported that CZTS and CZTSe can be synthesized as thin films, which use less material and decrease cost.[42] These materials also have shown a relatively high efficiency of 12.6% in solar energy conversion with a theoretical limit of 32%.[42,45,47,48] Due to these promising results, and the fact that a large number of I_2-II-IV-VI_4 quaternary DLSs can be investigated containing earth-abundant elements, research should continue in this area.

1.5.2 Nonlinear Optics

Nonlinear optics, first introduced in 1961, is a branch of optics that studies nonlinear interactions of light with matter.[49] Nonlinear optical (NLO) materials have utility in optical communications, laser medicine, and molecular spectroscopy.[21] Materials with the NLO property of second harmonic generation (SHG) are used in lasers to shift monochromic light to other wavelengths. SHG is a frequency doubling effect that occurs due to the nonlinear response of the compound.[49] In order for the fundamental energy to be transferred to the second-harmonic, the waves must be traveling at the same speed when going through the material.[49] There are several attractive NLO crystals for use in the visible and near-IR regions,[50,51] but there are less choices for applications deeper in the IR region of the electromagnetic spectrum[21,52] and no one material is operable over the entire region. Therefore, improved NLO materials for applications in the IR region are essential to advancing applications involving the remote sensing of chemical and biological weapons,[53] laser communication,[54] and the monitoring of air and water pollutants.[55]

An ideal SHG material should exhibit a large SHG coefficient, wide transparency region, high laser damage threshold (LDT), high thermal stability, phase matchability, and be easily synthesized as large single crystals.[56] However, the first criterion for a material to display a SHG response is that it must possess a noncentrosymmetric structure, which is true of all DLSs, since all of the tetrahedra point in the same direction along one crystallographic direction.[21] The inherently noncentrosymmetric structures of

DLSs along with their flexible compositions nominates them as ideal candidates for SHG applications. Consequently, ternary DLSs, such as $AgGaS_2$ and $AgGaSe_2$ are currently commercially available for SHG applications and are considered as benchmark IR NLO materials.[21,22] However, both of these compounds contain an increasingly non-abundant element, gallium, and multiphoton[57] absorption as well as relatively low LDTs[58] hinder their use in high-powered laser applications and generally affect laser performance.[21] Due to this, other DLSs with improved NLO properties are being investigated in the Aitken laboratory.

SHG materials that are active in the IR region are typically limited by high optical losses at short wavelengths due to poor transparency and low LDTs.[59-61] One way to increase LDT is to incorporate elements that can contribute a wider bandgap in the material.[62] Recently, quaternary materials including Li_2CdSnS_4, Li_2CdGeS_4, and Li_2ZnGeS_4 have been synthesized in the Aitken lab and have produced significant SHG responses and some of the most impressive LDTs to date.[23,59] Yet, other properties, such as thermal conductivity and crystal growth still need to be optimized. Having a variety of candidate quaternary DLSs to study for this purpose could be advantageous.

1.5.3 Thermoelectrics

Thermoelectric materials have seen an increase in attention due to their potential applications in power generation and electric cooling.[63,64] There are two types of thermoelectric devices, where one utilizes the Peltier effect and the other takes advantage of the Seebeck effect (Figure 1.3).[63] The Peltier effect is the basis for solid-state refrigeration, where an electrical current is applied across a thermoelectric junction of a device, which subsequently generates a temperature gradient.[65] In these materials, as a current is applied, it flows from the n-type material to the p-type material and the dominant carriers in both materials carry away heat as they move from the junction. As this occurs, the junction becomes cold as the electrical current carries the heat away. This effect can be seen in the use of thermoelectric devices in portable solid-state refrigerators or car seat heaters and coolers.[66,67] Thermoelectric materials that operate on the Seebeck effect convert thermal energy into electrical energy, opening up possible applications in waste heat recovery.[68] For example, thermoelectric devices can harvest energy from the waste heat that radiates from the exhaust system of an automobile.[66,69] In these devices, a temperature gradient is applied and electricity is generated. The heat is transported by the flow of the dominant carriers from the junction to the base, which generates a voltage between the two ends of the device.[63] However, in order for thermoelectric devices to realize their full potential, higher efficiencies are needed for use in large-scale applications such as home refrigeration and large-scale cooling/power generation.[69] The efficiency of a thermoelectric material is characterized by the dimensionless thermoelectric figure of merit (ZT), which is defined as:

$$ZT = (\sigma S^2/\kappa)T, \quad \text{(Eq. 1.5)}$$

where σ, S, κ, and T are the electrical conductivity, Seebeck coefficient, total thermal conductivity (the sum of its electronic, κe, and lattice, κ_L, contributions)[70], and absolute temperature, respectively.[71] However, finding a highly efficient thermoelectric material is a challenge because it requires the combination of a large Seebeck coefficient, high electrical conductivity, and low thermal conductivity, which are usually interrelated and often follow opposing trends.[72] Finding a material with a high figure of merit and suitable cost is also a challenge for researchers.[73]

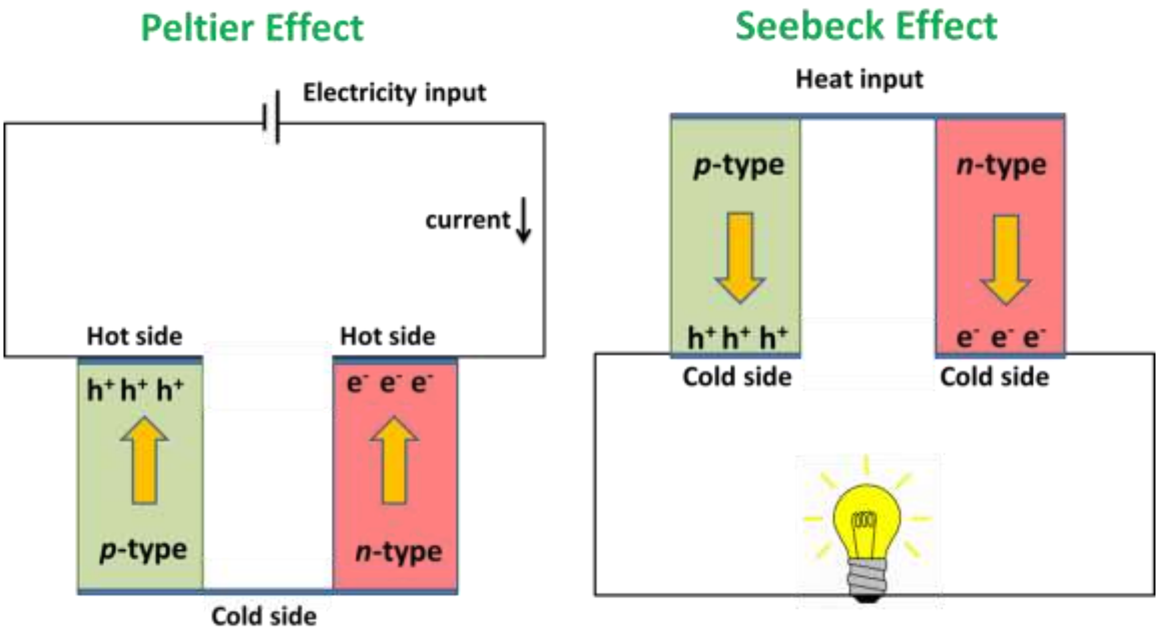

Figure 1.3. Schematic of a typical thermoelectric device displaying the Peltier effect (left) and the Seebeck effect (right).

Historically, the main approach to improve the ZT value of thermoelectric materials was to optimize bulk materials with relatively high ZT values, such as Bi_2Te_3, PbTe, and Si_xGe_y.[74] After the initial discovery of these materials, experimental efforts then turned to improving thermal and electrical transport by controlling the type and amount of doping to form solid solutions.[70,74] In order to increase the ZT values, these solid solutions have been used to reduce the lattice thermal conductivity through point defects resulting in the scattering of the phonons.[70] However, the introduction of point defects has led to the degradation of charge carrier mobility values, limiting the enhancement of ZT.[70] Kanatzidis et al. have reported Bi-doped SnTe with 3% HgTe to have a ZT of ~1.35 at 910 K, which is the highest figure of merit reported to date.[75]

Cu-based DLSs are relatively cheap, easy to make, and have shown potential in thermoelectric applications.[73] Recent tests on Cu-containing I_2-II-IV-VI_4 chalcogenides have shown relatively high ZT values, even though the compounds possess considerably wide bandgaps.[64] For example, the quaternary DLS $Cu_{2.1}Zn_{0.9}SnSe_4$ has demonstrated a thermoelectric figure of merit (ZT) of 0.91 at 850K.[71] The enhancement in ZT upon going from $Cu_2ZnSnSe_4$ to $Cu_{2.1}Zn_{0.9}SnSe_4$ can be explained by the amount of Cu in the structure of the material, as the Cu_2Se_4 units are considered as electrically conducting units.[64] The doping of Mn into Cu_2SnSe_3 and Cu into $Cu_2ZnGeSe_4$ has been investigated to increase ZT values.[73,76] Light doping (x=0.005) of Mn into Cu_2SnSe_3 has shown to decrease thermal conductivity and electrical resistivity due to an increased hole concentration.[73] The substitution of Cu for Zn into $Cu_2ZnGeSe_4$ also introduces holes as charge carriers and results in an enhancement of the thermoelectric efficiency.[76] The idea of doping is to increase the carrier concentration, which in turn increases the electrical conductivity.[73] In addition, the control of the composition allows for the tuning of the carrier concentration.[77] The substituted atoms can also serve to decrease the lattice thermal conductivity by distorting the normal crystal structures.[73,78] Furthermore, in the particular case of compositionally layered structures, for example stannite, high electrical conductivities can coexist with large Seebeck coefficients and intrinsically low thermal conductivities.[77] Thus, these compounds may be excellent thermoelectric materials and more work is needed to fully explore the potential of these materials.

1.6 Conclusion

This research focuses on the crystal structure, electronic structure, and physicochemical properties of several DLSs with the general formulae of I_2-II-IV-VI_4 and I_4-II-IV_2-VI_7. Regarding the I_2-II-IV-VI_4 stoichiometry, the focus is on the known compounds, $Cu_2ZnGeSe_4$ and $Cu_2MnGeSe_4$. However, even though these compounds are known there is limited data reported about their optical and thermoelectric properties. Research into these I$_2$-II-IV-VI$_4$ compounds led to the serendipitous discovery of a new compound, $Cu_4ZnGe_2Se_7$. This prompted further investigations into the family of I$_4$-II-IV$_2$-VI$_7$ structures, specifically Cu$_4$-II-Ge$_2$-Se$_7$ where II = Mn, Fe, Co, Ni, and Zn, leading to the identification of several new phases. This work describes the relationships between the I$_2$-II-IV-VI$_4$ and the I$_4$-II-IV$_2$-VI$_7$ structures, along with the similarities and differences in the resulting physicochemical properties.

2. Synthesis and Characterization of $Cu_2ZnGeSe_4$, $Cu_2MnGeSe_4$, and $Cu_4ZnGe_2Se_7$

2.1 Introduction

The initial goal of this work was to prepare $Cu_2ZnGeSe_4$ and $Cu_2MnGeSe_4$ as phase-pure materials. After synthesis, X-ray powder diffraction (XRPD) analysis was performed to assess the purity of the compounds and synthesis techniques were altered until phase-purity was achieved. Single crystal X-ray diffraction led to the unforeseen discovery of a new compound, $Cu_4ZnGe_2Se_7$. Once these compounds were synthesized phase-pure, their electronic structures and physicochemical properties were characterized and compared. The investigation of both the crystal and electronic structures of quaternary DLSs is essential in understanding the origin of the physicochemical properties and formulating structure-property and composition-property correlations. This chapter explains in detail the methods and procedures of the synthesis and characterization techniques that were performed.

2.2 Experimental Details and Procedures

2.2.1 Reagents

Copper powder, 99.999%, Strem, Newburyport, MA; germanium powder, 99.999%, Strem Newburyport, MA; manganese powder, 99.999%, Strem Newburyport, MA; selenium powder, 99.99%, Strem, Newburyport, MA; zinc powder, 99.999%, Strem, Newburyport, MA were used without further purification.

2.2.2 Synthesis of $Cu_2ZnGeSe_4$, $Cu_2MnGeSe_4$, and $Cu_4ZnGe_2Se_7$

High-temperature, solid-state synthesis was performed to obtain phase-pure powders of $Cu_2ZnGeSe_4$, $Cu_2MnGeSe_4$, and $Cu_4ZnGe_2Se_7$. Stoichiometric amounts of Cu, Mn, Zn, Ge, and Se were weighed out in mmol quantities in a glove box under argon. Initially, each reactant mixture was ground with a mortar and pestle and then placed into a 9 mm outer diameter fused-silica tube. The samples were then removed from the glove box and flamed-sealed under a vacuum of approximately 10^{-3} mbar using an oxy-methane torch. However, due to a small amount of starting materials sticking to the sides of the tube, a reaction with the fused-silica tube at high temperature occurred during flame-sealing, making the tube difficult to properly seal. To avoid this, a smaller 9 mm outer diameter fused-silica tube containing the reactants was placed into a larger 12 mm outer diameter fused-silica tube before sealing. To increase phase purity, three minor synthesis adjustments were implemented including: 1) no grinding of the elemental starting materials before being placed in the reaction tubes, 2) addition of 5 % excess selenium to maintain stoichiometry and to reduce the formation of vacancies in the sample,[34] and 3) doubling of the reaction to reduce the significance of the errors in measuring the masses of starting materials. $Cu_2ZnGeSe_4$, $Cu_2MnGeSe_4$, and $Cu_4ZnGe_2Se_7$ were all synthesized with these adjustments, each adjustment individually and then a reaction employing a combination of all three. The sealed tubes were then placed in a furnace and heated to 800 °C in 12 h and held at that temperature for 192 h for the $Cu_2ZnGeSe_4$ and the $Cu_2MnGeSe_4$ samples and for 96 h for the $Cu_4ZnGe_2Se_7$ samples. The samples were then cooled to 400 °C in 53 h, at a rate of 7.5 °C/h and then cooled to ambient temperature. XRPD patterns, shown in Chapter 3, will illustrate that $Cu_2ZnGeSe_4$ and $Cu_2MnGeSe_4$ were able to be synthesized phase-pure by using excess selenium, whereas $Cu_4ZnGe_2Se_7$ was synthesized nearly phase-pure with no grinding.

2.2.3 Single Crystal Structure Determination

A Bruker SMART Apex II CCD single crystal X-ray diffractometer employing graphite monochromatized molybdenum K_α radiation with a wavelength of 0.7107 Å and operating with a tube power of 50 kV and 30 mA was used to collect the data for a rod crystal of $Cu_4ZnGe_2Se_7$ at 40 s/frame at ambient temperature. A total of 4254 reflections were collected with 1344 of them being unique. The program SAINT[79] was used to integrate the data and SADABS[80] was employed to perform the absorption correction. XPREP was used for space group determination and to create files for SHELXTL.[81] After full integration, a new structure solved and refined for the new compound $Cu_4ZnGe_2Se_7$. Based on systematic absences, two space groups were considered, *C*2 and *C*2/*m*. However, since all DLSs have noncentrosymmetric structures due to the alignment of all tetrahedra in one crystallographic direction, the space group *C*2 was used to solve the monoclinic structure of $Cu_4ZnGe_2Se_7$. All atoms were refined anisotropically. The Flack parameter of 0.10(4) for $Cu_4ZnGe_2Se_7$ is close to zero, which indicates that the absolute structure is correct. All crystal structure figures were generated using CrystalMaker®. The final refinement statistics and crystallographic details are provided in Chapter 3 along with the atomic coordinates, selected bond distances and angles, and isotropic atomic displacement parameters.

2.2.4 X-ray Powder Diffraction (XRPD)

X-ray powder diffraction data were collected using a PANalytical X'Pert Pro MPD X-ray powder diffractometer with an X'cellerator detector in Bragg–Brentano geometry. The instrument, operating with a tube power of 45 kV and 40 mA, employed Ni-filtered, copper Kα radiation with a wavelength of 1.541871 Å. Data were collected as a continuous scan from 10 to 80° 2θ in increments of 0.08° over the course of 1 h. A 0.25° divergence slit, 0.5° anti-scatter slit, and a 0.02 rad Soller slit were used for both the incident and diffracted beam optics. The samples were prepared for measurement by grinding the crystals in a mortar and pestle for 30 minutes. The powdered samples were then placed onto glass slides, positioned in sample holders and loaded into the instrument for data collection. Phase identification was performed using X'pert High ScorePlus[82] and the International Centre for Diffraction Data (ICDD) powder diffraction file (PDF) database.

2.2.5 High-Resolution Synchrotron X-ray Powder Diffraction (SXRPD) and Rietveld Refinements

Due to the fact that the reference patterns for $Cu_2ZnGeSe_4$ and $Cu_4ZnGe_2Se_7$ are so similar to one another and potential ternary and binary secondary phases, it is hard to distinguish between them using laboratory-grade X-ray powder diffraction data. Therefore, high-resolution, high-intensity synchrotron powder diffraction data (SXRPD) were collected at room temperature using beamline 11-BM at the Advanced Photon Source (APS), Argonne National Laboratory using an average wavelength of 0.413838 Å. This shorter wavelength provides much better resolution than laboratory X-ray powder diffraction, which uses copper K_α radiation with a wavelength of 1.54187 Å. This will help to differentiate between $Cu_2ZnGeSe_4$ and $Cu_4ZnGe_2Se_7$ phases and to identify peaks, which may appear overlapped in the laboratory-grade data. Additionally, the high flux of the source provides very intense diffraction patterns allowing one to see peaks that are normally too small to distinguish from background in the laboratory-grade data. The 11-BM instrument uses X-ray optics with two platinum-stripped mirrors and a double-crystal Si(111) monochromator, with the second crystal having an adjustable sagittal bend.[83] Ion chambers monitor incident flux. A vertical Huber 480 goniometer, equipped with a eidenhain encoder, positions an analyzer system comprised of twelve perfect Si(111) analyzers and twelve Oxford-Danfysik $LaCl_3$ scintillators, with a spacing of 2º 2θ.[84] The samples were spun during data collection. A Mitsubishi robotic arm was used to mount and dismount the samples on the diffractometer.[85] Detectors covering an angular range from -6 to 16º 2θ were scanned over a 34º 2θ range, with data points collected every 0.001º 2θ and a scan speed of 0.01º/s. The diffractometer was controlled via EPICS.[86] Data were collected while continually scanning the diffractometer 2θ arm. A mixture of NIST standard reference materials, Si (SRM 640c) and Al_2O_3 (SRM 676) was used to calibrate the instrument, where the Si lattice constant determines the wavelength for each detector. Corrections were applied for detector sensitivity, 2θ offset, small differences in wavelength between detectors, and the source intensity, as noted by the ion chamber before merging the data into a single set of intensities evenly spaced in 2θ.

Rietveld refinements were conducted using the General Structure Analysis System (GSAS) with EXPGUI.[87] The known crystal structure of $Cu_2ZnGeSe_4$ in space group *I*-42*m*[88] was obtained from the International Crystal Structure Database (ICSD), code number 93409, and used as a starting model for the refinement. The starting model for $Cu_4ZnGe_2Se_7$ was the crystal structure (*C*2*)* obtained using single crystal X-ray diffraction. A shifted Chebyshev polynomial was used for background correction,[89] and peak shapes were modeled using Lorentzian isotropic crystallite size broadening (LX) and Lorentzian isotropic strain broadening (LY) terms within the type-3 profile function. Lattice parameters, atomic coordinates, and isotropic displacement parameters were refined. The structural data obtained from Rietveld refinement, including unit cell parameters, atomic coordinates, atomic displacement parameters, and bond lengths and angles shown in Chapter 3, were in good agreement with those obtained using single crystal X-ray diffraction.

2.2.6 Scanning Electron Microscopy and Energy Dispersive Spectroscopy (SEM/EDS)

Semi-quantitative elemental analysis for $Cu_2ZnGeSe_4$, $Cu_2MnGeSe_4$ and $Cu_4ZnGe_2Se_7$ was executed using a Hitachi S-3400 N scanning electron microscope equipped with a Bruker Quantax model 400 energy dispersive spectrometer using an XFlash® 5010 EDS detector with a 129 eV resolution. Single crystals of $Cu_2ZnGeSe_4$, $Cu_2MnGeSe_4$ and $Cu_4ZnGe_2Se_7$ were attached to double-sided carbon tape that was adhered onto an aluminum specimen holder. Three crystals of each sample were selected for semi-quantitative EDS analysis. EDS spectra were collected for three areas on each crystal at an accelerating voltage of 15 kV for 5 min live time at a working distance of 10 mm. This data were used to determine the elemental ratio of the samples to further confirm the synthesis of the target compounds.

2.2.7 Inductively Coupled Plasma Optical Emission Spectroscopy (ICP-OES)

Quantitative analysis of Cu, Zn, Ge, and Se was performed by RJ Lee Group Inc. in Monroeville, PA using inductively coupled plasma optical emission spectroscopy (ICP-OES). Approximately 50 mg of both $Cu_2ZnGeSe_4$ and $Cu_4ZnGe_2Se_7$ were used for analysis. Samples were prepared for analysis by microwave-assisted acid digestion in high-pressure XP1500 vessels with a MarsExpress CEM Microwave system. The digested samples were analyzed in a Varian 730ES ICP-OES for Cu, Zn, Ge, and Se.

2.2.8 Optical Diffuse Reflectance UV/Vis/NIR Spectroscopy

A Varian Cary 5000 spectrometer, equipped with a Harrick Praying Mantis diffuse reflectance accessory, was used to collect the optical diffuse reflectance spectra of the $Cu_2ZnGeSe_4$, $Cu_2MnGeSe_4$, and $Cu_4ZnGe_2Se_7$ over the ultraviolet, visible, and near infrared spectral regimes (UV/VIS/NIR). Each sample was ground and placed into a sample holder to a depth of 3 mm. Barium sulfate (Fisher, 99.92%) was used as a 100% reflectance standard. The measurement was conducted at a scan rate of 600 nm/min. Using the Kubelka-Munk transformation, $\alpha_{KM} / s = (1-R)^2/(2R)$, the raw reflectance (R) was converted to relative absorption (α_{KM}) since the scattering coefficient, s, is unknown.[90] The Urbach energy was obtained by fitting the optical data to the functional form $\alpha= A*\exp(E-E_g/E_u)$, where A is a constant, E is the photon energy in eV, E_g is the bandgap energy, and E_u is the Urbach energy.[91] These calculations along with the estimation of the Urbach tail were implemented to determine the bandgaps of the targeted materials. The fits for the direct bandgaps of these materials will be described in Chapter 3.

2.2.9 Attenuated Total Reflectance (ATR) FT-IR Spectroscopy

Diffuse reflectance UV-visible-NIR spectroscopy was used in conjunction with attenuated total reflectance (ATR) FT-IR spectroscopy to assess the windows of optical clarity for $Cu_2ZnGeSe_4$ and $Cu_4ZnGe_2Se_7$. Infrared spectra for these compounds were collected using a Thermo Nicolet 380 FT-IR spectrometer equipped with an attenuated total reflectance (ATR) accessory. The IR spectra are comprised of 64 scans from 400 cm^{-1} to 4000 cm^{-1}. The OMNIC software was used for data collection and analysis. The FT-IR system uses a diamond crystal in optical contact with the sample. Thus, the depth of penetration into the sample is ~2 μm, which is near the lower limit of the particle sizes for the samples. Therefore, the effect of thickness dependence on the intensity of the measured spectra is negligible.[92]

2.2.10 Differential Thermal Analysis (DTA)

DTA data for $Cu_2ZnGeSe_4$ and $Cu_4ZnGe_2Se_7$ were collected using a Shimatzu DTA-50 differential thermal analyzer. Data were recorded using the TA60-WS collection program. Calibration of the instrument was performed using a three-point calibration curve based on the melting points of indium, zinc and gold metals. Approximately 20 mg of each sample was sealed in a carbon-coated, fused-silica ampoule and flame-sealed under a vacuum of ~10^{-3} mbar. The sample and the reference material, Al_2O_3, of comparable mass were heated at a rate of 10 °C /min from 25 °C to 1000 °C under a constant flow of nitrogen gas, held at the high temperature for 1 min and cooled at a rate of 10 °C/min to 100 °C. Two cycles were performed in order to distinguish reversible and irreversible events

2.2.11 Electronic Structure Calculations

Electronic structure calculations, band structure and density of states (DOS), as well as a quantitative bond analysis for both $Cu_2ZnGeSe_4$ and $Cu_4ZnGe_2Se_7$ were performed using the total-energy code of CASTEP.[93,94] In CASTEP, the total energy is calculated using the plane-wave pseudopotential method of density functional theory (DFT). The Perdew, Burke, and Ernzerhof generalized gradient approximation (PBE-GGA) was used to treat the exchange and correlation effects.[95] In this method, the interactions between the ionic cores and the electrons are described by norm-conserving pseudopotentials.[96] The following orbitals were treated as valance electrons: Cu $3p^6 3d^{10} 4s^1$, Zn $3p^6 3d^{10} 4s^2$, Ge $4s^2 4p^2$, and Se $4s^2 4p^4$. The number of plane-waves included in the basis set was determined by an energy cutoff of 800 eV and the numerical integration of the Brillouin zone was performed using a 5x5x6 and a 3×3×3 Monkhorst-Pack k-point sampling for $Cu_2ZnGeSe_4$ and $Cu_4ZnGe_2Se_7$ respectively. The total energy converged to 1×10^{-6} eV/atom in the self-consistent field (SCF) by using 100 cycle calculations. Default values of the CASTEP code were taken for the remaining parameters. The bond orders were then calculated using a Mulliken bond population analysis within the CASTEP code.[97,98]

3. Results and Discussion

3.1 Introduction

Due to the potential uses in applications, such as solar cells, nonlinear optics, and thermoelectrics, it is imperative to fully characterize the two quaternary DLSs of the I_2-II-IV-VI_4 family, $Cu_2ZnGeSe_4$ and $Cu_2MnGeSe_4$, which were prepared by high-temperature, solid-state synthesis. Numerous heating profiles and synthetic techniques were employed to produce phase-pure compounds. Investigations to prepare these I_2-II-IV-VI_4 diamond-like semiconductors, specifically $Cu_2ZnGeSe_4$, led to the serendipitous finding of a new compound, $Cu_4ZnGe_2Se_7$, which in turn prompted the exploration and discovery of a new family of materials with distorted diamond-like structures having the formula I_4-II-IV_2-VI_7. Characterization of $Cu_2ZnGeSe_4$, $Cu_2MnGeSe_4$, and $Cu_4ZnGe_2Se_7$ was performed using a number of techniques, as described in Chapter 2. This chapter discusses the results of these investigations, while preliminary findings on $Cu_4MnGe_2Se_7$, $Cu_4FeGe_2Se_7$, $Cu_4CoGe_2Se_7$, and $Cu_4NiGe_2Se_7$ are detailed in the appendix.

3.2 Results

3.2.1 Single Crystal Determination

$Cu_2ZnGeSe_4$ is a known compound that adopts the stannite structure with the space group $I\text{-}42m$ and is made up of alternating cation layers (Figure 3.1).[34] There are four crystallographically unique atoms in its structure; 1 Cu, 1 Zn, 1 Ge, and 1 Se. Throughout the structure, layers of alternating Zn and Ge cations are separated by layers of Cu cations as shown in Figure 3.2. In its local coordination spehere each selenium anion is nearly the same, being tetrahedrally surrounded by four nearest-neighbor metal cations, two copper cations, one zinc cation, and one germanium cation at the corners of the surrounding tetrahedron, resulting in local charge neutrality. More specifically, the structure of $Cu_2ZnGeSe_4$ is comprised of selenium anions in a cubic-closest-packed array, with copper, zinc, and germanium all together occupying half of the tetrahedral holes. Each cation in $Cu_2ZnGeSe_4$ coordinates to four tetrahedral selenium anions, and all of the tetrahedra align along the c-axis rendering the structure noncentrosymmetric (Figure 3.3)

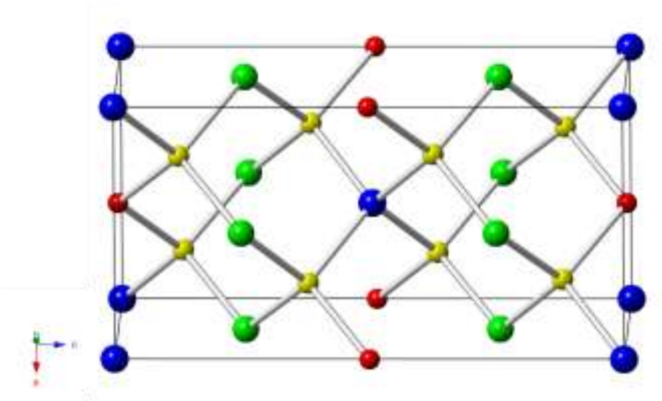

Figure 3.1. The unit cell of $Cu_2ZnGeSe_4$ viewed down the crystallographic b-axis. Color code: Cu = green, Zn = blue, Ge = red, and Se = yellow.

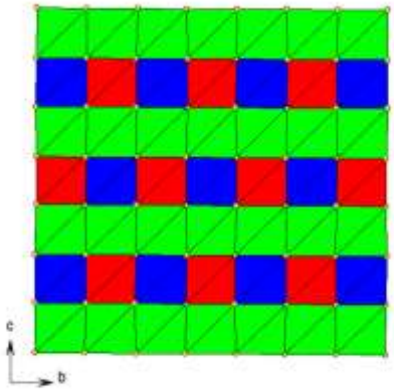

Figure 3.2. The cation ordering pattern in $Cu_2ZnGeSe_4$ is composed of layers of alternating Zn and Ge cations, running along the b-axis, that are separated by layers of Cu atoms. Color code: Cu = green, Zn = blue, and Ge = red.

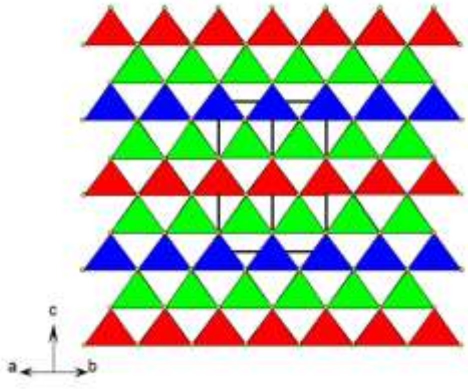

Figure 3.3. The tetrahedra align along the c-axis in $Cu_2ZnGeSe_4$ rendering the structure noncentrosymmetric. Color code: Cu = green, Zn = blue, and Ge = red.

$Cu_4ZnGe_2Se_7$ is a new compound that crystallizes in the monoclinic space group *C*2 (Figure 3.4). There are eight crystallographically unique atoms in its structure; 2 Cu cations, 1 Zn cation, 1 Ge cation, and 4 Se anions. As in the case of $Cu_2ZnGeSe_4$, each cation in $Cu_4ZnGe_2Se_7$ coordinates to four tetrahedral selenium anions, and all of the tetrahedra align along the c-axis making the structure noncentrosymmetric. Also similar to $Cu_2ZnGeSe_4$, the structure of $Cu_4ZnGe_2Se_7$ is comprised of selenium anions packed into a cubic-closest-packed array, with copper, zinc, and germanium occupying half of the tetrahedral holes; however, the pattern of the cations differs. Throughout the structure, $CuSe_4$ tetrahedra are connected to each other to form a 2D layer in the *bc* plane. Adjacent layers of CuSe are further connected into a 3D CuSe framework (Figure 3.5). Zn and Ge cations are located in the interspace of the 3D CuSe framework and also connect to four selenium anions (Figure 3.6). Selected crystallographic data for $Cu_4ZnGe_2Se_7$ is shown in Table 3.1. Atomic coordinates, isotropic atomic displacement parameters and bond lengths and angles are displayed in Tables 3.2 and 3.3.

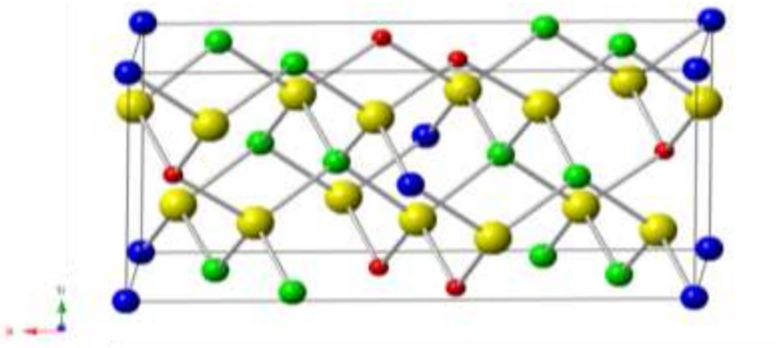

Figure 3.4. The unit cell of $Cu_4ZnGe_2Se_7$ viewed down the crystallographic c-axis. Color code: Cu = green, Zn = blue, Ge = red, and Se = yellow.

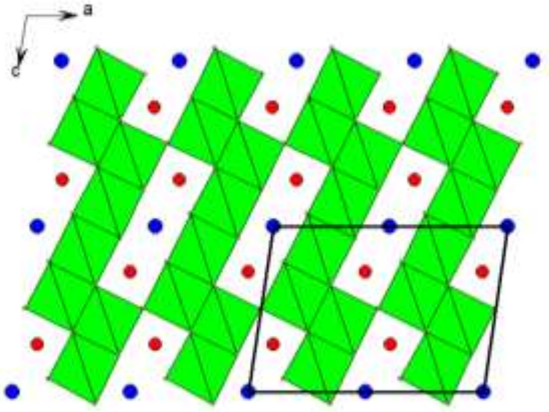

Figure 3.5. The 3D $[Cu_4Se_7]^{6-}$ framework with Zn^{2+} and Ge^{4+} cations in the interspace. Color code: Cu = green, Zn = blue and Ge = red.

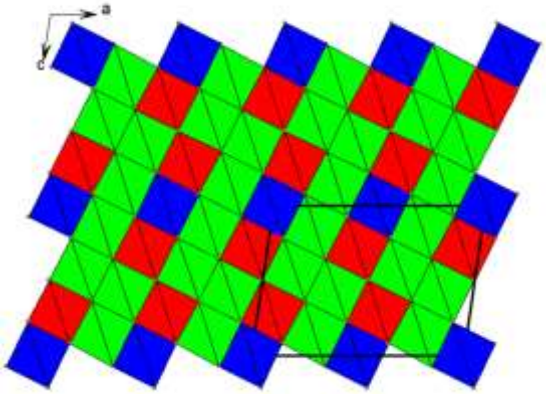

Figure 3.6. 3D tetrahedral view of $Cu_4ZnGe_2Se_7$. Color code: Cu = green, Zn = blue and Ge = red.

Table 3.1. Crystallographic data and experimental details for $Cu_4ZnGe_2Se_7$.

Formula	$Cu_4ZnGe_2Se_7$
Size (mm)	0.23 × 0.03 × 0.02
Temperature (K)	296(2)
Space group, No.	*C*2, 5
a (Å)	12.3443(4)
b (Å)	5.6195(2)
c (Å)	8.7904(3)
β (°)	98.693(2)
Volume ($Å^3$), Z	602.77(4), 2
Density (Mg/m^3)	5.606
Reflections collected/unique	4254/1344
Data/Restraints /Parameters	1344/1/67
Completeness to theta = 27.11°	100.0 %
Goodness of fit	1.079
Final R indices [$I>2\sigma(I)$]	R1 = 0.0301, wR_2 = 0.0778
R indices (all data)	R1 = 0.0337, wR_2 = 0.0808
Highest peak, deepest hole (e/$Å^3$)	0.834, -1.333
Refinement of F^2 was made against all reflections. $R_1 = (\Sigma\|\|F_o\|-\|F_c\|\|)/(\Sigma\|F_o\|)$, $wR_2 = \sqrt{(\Sigma[w(F_o^2-F_c^2)^2]/\Sigma[w(F_o^2)^2])}$, $w = 1/(\sigma^2(F_o^2) + (aF_o)^2 + bP)$, $P = [2F_c^2 + Max(F_o^2,0)]/3$	

Table 3.2. Atomic coordinates and isotropic displacement parameters (U_{iso}) obtained from single crystal data of $Cu_4ZnGe_2Se_7$.

Site	**Multiplicity Wyckoff Letter**	**x**	**y**	**z**	**U_{iso} Å^2**
Cu1	4c	0.14283(6)	0.0149(3)	0.4356(1)	0.0199(4)
Cu2	4c	0.2114(6)	0.5059(3)	0.14315(8)	0.0161(4)
Zn1	2a	0.0000	0.0026(3)	0.0000	0.0232(6)
Ge1	4c	0.42671(4)	0.9910(3)	0.28255(7)	0.0109(3)
Se1	2b	0.0000	0.7475(1)	0.5000	0.0110(4)
Se2	4c	0.06979(4)	0.2526(2)	0.21764(8)	0.0123(4)
Se3	4c	0.28240(5)	0.7654(2)	0.35450(6)	0.0109(3)
Se4	4c	0.35718(5)	0.2525(2)	0.07810(9)	0.0120(3)

Table 3.3. Bond distances (Å) and angles (°) from single crystal data of $Cu_4ZnGe_2Se_7$.

Cu1—Se3i	2.392(2)	Se3i—Cu1—Se2	110.06(8)
Cu1—Se2	2.398(1)	Se3i—Cu1—Se3ii	111.14(3)
Cu1—Se3ii	2.411(2)	Se2—Cu1—Se3ii	106.66(4)
Cu1—Se1	2.447(1)	Se3i—Cu1—Se1	112.99(4)
		Se2—Cu1—Se1	109.26(3)
		Se3ii—Cu1—Se1	106.47(8)
Cu2—Se2	2.418(1)	Se2—Cu2—Se3	109.89(3)
Cu2—Se3	2.421(2)	Se2—Cu2—Se4	108.06(8)
Cu2—Se4	2.432(1)	Se3—Cu2—Se4	109.69(4)
Cu2—Se4iii	2.433(1)	Se2—Cu2—Se4iii	112.01(3)
		Se3—Cu2—Se4iii	108.18(8)
		Se4—Cu2—Se4iii	108.98(3)
Zn1—Se2iv	2.425(1)	Se2iv—Zn1—Se2	109.17(9)
Zn1—Se2	2.425(1)	Se2iv—Zn1—Se4v	111.78(2)
Zn1—Se4v	2.433(1)	Se2—Zn1—Se4v	107.35(2)
Zn1—Se4vi	2.433(1)	Se2iv—Zn1—Se4vi	107.35(2)
		Se2—Zn1—Se4vi	111.79(2)
		Se4v—Zn1—Se4vi	109.45(9)
Ge1—Se3	2.350(1)	Se3—Ge1—Se2vii	112.66(8)
Ge1—Se2vii	2.355(1)	Se3—Ge1—Se4viii	109.57(3)
Ge1—Se4viii	2.379(1)	Se2vii—Ge1—Se4viii	111.50(3)
Ge1—Se1ix	2.455(1)	Se3—Ge1—Se1ix	108.20(3)
		Se2vii—Ge1—Se1ix	108.73(3)
		Se4viii—Ge1—Se1ix	105.89(8)

Symmetry codes: (i) $-x+1/2$, $y-1/2$, $-z+1$; (ii) x, $y-1$, z; (iii) $-x+1/2$, $y+1/2$, $-z$; (iv) $-x$, y, $-z$; (v) $x-1/2$, $y-1/2$, z; (vi) $-x+1/2$, $y-1/2$, $-z$; (vii) $x+1/2$, $y+1/2$, z; (viii) x, $y+1$, z; (ix) $x+1/2$, $y+3/2$, z.

When comparing the crystal structures of $Cu_2ZnGeSe_4$ and $Cu_4ZnGe_2Se_7$ both have a Z of 2, which means they each have twice as many atoms in their unit cell as in their formula (Ex: $Cu_2ZnGeSe_4$ actually is $Cu_4Zn_2Ge_2Se_8$ when considering the total unit cell contents). However, $Cu_4ZnGe_2Se_7$ does not obey Pauling's 2nd rule because not all of the four crystallographically unique selenium atoms have their charge satisfied by the cations in the first coordination sphere as seen in Figure 3.7. An extended connectivity table based on the unit cell contents with horizontal and vertical bond strength sums for each crystallographically unique cation and anion in $Cu_4ZnGe_2Se_7$ is shown in Table 3.4. All of the cations in $Cu_4ZnGe_2Se_7$ are charge balanced with the Se anions around them. Yet, Se(1) has a vertical bond strength sum of 5 instead of 4 and Se(3) has a vertical bond strength of 7 instead of 8.

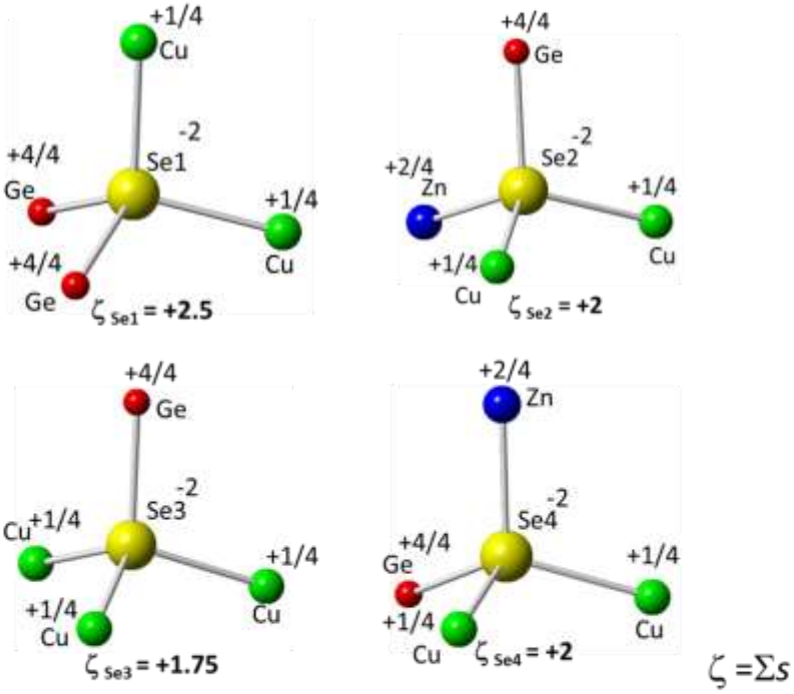

Figure 3.7. The four crystallographically unique selenium atoms in $Cu_4ZnGe_2Se_7$. Pauling's 2nd rule is not satisfied for Se(1) and Se(3).

Pauling's 2^{nd} rule states that the charge of the anion should be compensated by the cations that are directly bound to it. While Se(2) and Se(4) in this structure are in accordance with Pauling 2^{nd} rule, having two copper, one zinc and one germanium cation as nearest neighbors, Se(1) and Se(3) are not in satisfaction of local charge neutrality. Se(1) is bound to two Cu(1) cations and two Ge(1) cations. Therefore, the charge of Se(1) is overcompensated by 0.5. When local charge is not compensated, the polyhedra will undergo distortions to alleviate the charge imbalance. Se(1) responds to this environment by lengthening the bonds with the cations. Se(1) has the largest average cation-Se distance in the structure. The Se(1)-Cu(1) distances are 2.447(1) Å, the longest Cu-Se distances in the structure. Likewise the Se(1)-Ge(1) distances are 2.455(1) Å, ~0.08 Å longer than the next shortest Se-Ge bond distance. The charge of the Se(3) atom is undercompensated by 0.25, with two Cu(1) cations, one Cu(2) cation and one Ge(1) cation in its first coordination sphere. The average cation-Se(3) bond distance is the shortest in the structure by only a small amount. Even with an overcompensation of 0.50 by Se(1) and an under compensation of 0.25 by Se(3), there will still be global charge balance because Se(1) is on a special position. Due to this, there are only half as many Se(1) atoms in the unit cell compared to the other selenium atoms. When this multiplicity is taken into account and the residual charges are added up for each selenium atom in the unit cell (Table 3.5), the structure globally charge balances, even though Pauling's 2^{nd} rule is not satisfied for each selenium atom individually.

Table 3.4. Extended connectivity table based on the unit cell contents with horizontal and vertical bond strength sums for each crystallographically unique cation (horizontal) and anion (vertical) in $Cu_4ZnGe_2Se_7$.

	2 Se(1)	4 Se(2)	4 Se(3)	4 Se(4)	
4 Cu(1)	4 × ¼	4 × ¼	8 × ¼		$\Sigma = 4 = 4ve_{Cu}$
4 Cu(2)		4 × ¼	4 × ¼	8 × ¼	$\Sigma = 4 = 4ve_{Cu}$
2 Zn(1)		4 × ½		4 × ½	$\Sigma = 4 = 2ve_{Zn}$
4 Ge(1)	4 × 1	4× 1	4 × 1	4 × 1	$\Sigma = 16 = 4ve_{Ge}$
vertical bond strength sum	$\Sigma = 5$ $(5 > 4)$	$\Sigma = 8$	$\Sigma = 7$ $(7 < 8)$	$\Sigma = 8$	
Ideal bond strength sum	$4 = 2(8-ve_S)$	$8 = 4(8-ve_S)$	$8 = 4(8-ve_S)$	$8 = 4(8-ve_S)$	

Table 3.5. Analysis of the charge on each selenium atom in $Cu_4ZnGe_2Se_7$.

Crystallographically Unique Se	**Multiplicity in Unit Cell**	**Residual Local Charge per Se atom**	**Overall Charge of each Se in Unit Cell**
Se1	SPECIAL POSITON 2	+0.5	2 x +0.5 = +1
Se2	4	0	4 x 0 = 0
Se3	4	-0.25	4 x -0.25 = -1
Se4	4	0	4 x 0 = 0

However, despite the noncompliance of $Cu_4ZnGe_2Se_7$ with Pauling's 2nd rule, the disparities between bond lengths and angles of the tetrahedra in $Cu_2ZnGeSe_4$ and $Cu_4ZnGe_2Se_7$ are subtle; yet, the ordering patterns of the tetrahedra are strikingly dissimilar (Figure 3.8). In $Cu_2ZnGeSe_4$, rows of alternating Zn and Ge cations are separated by rows of Cu cations. In $Cu_4ZnGe_2Se_7$, each row contains a mixture of Zn, Ge, and Cu cations, where the Zn and Ge cations are separated by Cu cations in that row. When compared to $Cu_2ZnGeSe_4$, each row stacks together in a more complicated way, whereas in each column, cations are in an order of Ge (red), Zn (blue), Ge (red), Cu (green), Cu (green), Cu (green), Cu (green), Cu (green).

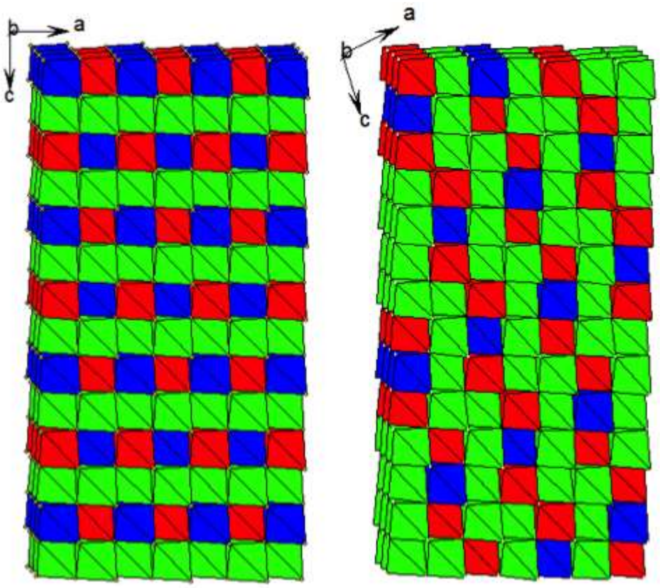

Figure 3.8. Cation ordering patterns in $Cu_2ZnGeSe_4$ (left) and $Cu_4ZnGe_2Se_7$ (right). Color code: Cu = green, Zn = blue and Ge = red.

Due to the presence of more copper in the compound and the more distorted diamond-like structure that results from the violation of Pauling's 2nd rule,[29] $Cu_4ZnGe_2Se_7$ may be better suited than $Cu_2ZnGeSe_4$ for the aforementioned applications, especially in thermoelectrics. This additional copper serves to connect the electrical conducting units (ECUs) in the structure.[20] This can be explained by the decoupling of the electrical and thermal transport properties in the material to enhance ZT.[99] The structure and composition of $Cu_4ZnGe_2Se_7$ naturally serves to increase the ECUs in the structure. Depiction of the Cu-Se framework in $Cu_2ZnGeSe_4$ reveals a 2-D structure while that in $Cu_4ZnGe_2Se_7$ is 3-D (Figure 3.9).

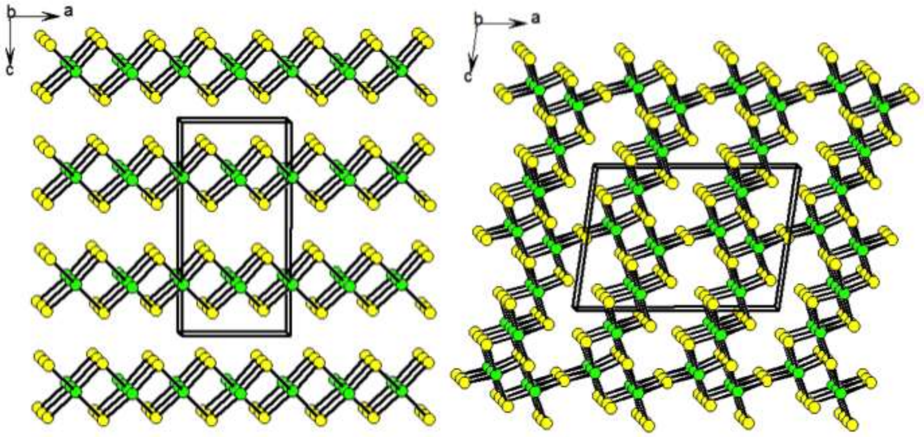

Figure 3.9. The structures of $Cu_2ZnGeSe_4$ (left) and $Cu_4ZnGe_2Se_7$ (right) showing only the Cu-Se frameworks. Color code: Cu = green and Se = yellow.

3.2.2 X-ray Powder Diffraction (XRPD)

$Cu_2ZnGeSe_4$ and $Cu_2MnGeSe_4$ have been previously synthesized and partially characterized in other works.[7,36,37] The synthesis involved direct combination in an argon-filled glove box in which the reagents were ground and added to fused-silica tubes. In this process, stoichiometric ratios of the elements were weighed out in millimolar ratios. After being removed from the glove box, the tubes were flame sealed on a vacuum line

($\sim10^{-3}$ mbar) and then placed into a programmable furnace. Previous reports failed to give a specific heating profile; therefore, multiple heating procedures were tested in this work, as described in Chapter 2. Initially, two different heating profiles were used, one with a maximum temperature of 800 °C and one with a maximum temperature of 700 °C. Each had a hold time of 4 days (96 hours) at that maximum temperature with a constant temperature decrease of 7.5 °C/h to 400 °C. The furnace was then rapidly cooled to room temperature in 3hs.

After coming out of the furnace, the reaction products were ground and characterized by X-ray powder diffraction (XRPD) to determine their phase purity. The collected X-ray powder diffraction patterns were then compared to the reference patterns and the patterns of possible secondary phases obtained from the powder diffraction file to determine which reaction gave the most phase-pure products. However, it was difficult to conclude if the product that was made was the intended quaternary product or a mixture of ternary and binary phases because all of them have very similar X-ray powder diffraction patterns, since many of the potential binary and ternary impurity phases also possess diamond-like structures. Figure 3.10 shows an example of collected data that is compared to the reference patterns of possible impurity phases. Upon closer inspection of all of the observed diffraction patterns, a distinguishable peak was noted at ~17° 2θ which is indicative of the I_2-II-IV-VI_4 structure, thus suggesting the desired product was synthesized (Figure 3.11).

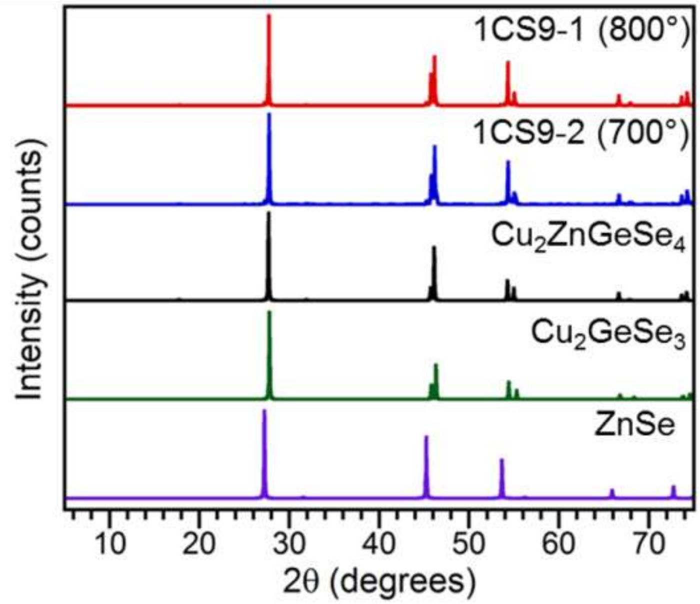

Figure 3.10. XRPD patterns of reactions intended to produce $Cu_2ZnGeSe_4$ compared to reference XRPD patterns obtained from the powder diffraction file (PDF) database.[88]

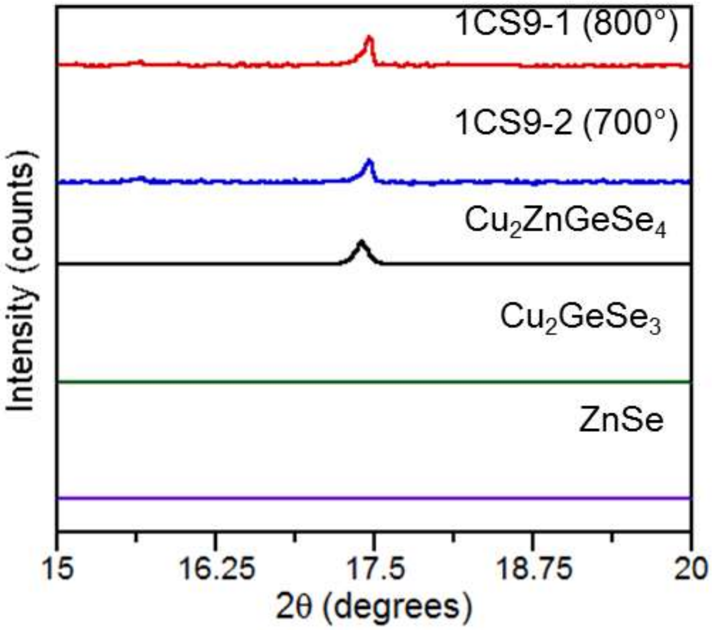

Figure 3.11. A distinguishable peak at ~17° 2θ which only appears in the I_2-II-IV-VI_4 reference pattern was used to confirm that the material was synthesized.

After thorough examination of the XRPD patterns, it could be seen that the reactions performed with a maximum temperature of 800 °C for 4 days had less secondary phases, yet some were still present as shown in Figures 3.12 and 3.13. Therefore, the heating profile needed to be optimized to obtain phase-pure compounds. This is important because phase-pure compounds are necessary for characterization, making the interpretation of data from various physicochemical characterization techniques more straightforward and less ambiguous. Multiple heating profiles with higher maximum temperatures, including 850 °C, and longer hold times of up to 2 weeks were tested. After these samples came out of the furnaces, XRPD was performed to determine which of the new heating profiles provided less secondary phases and even though small impurity peaks were still present, it was clear that the profile for the sample with a maximum synthesis temperature at 800 °C for 8 days best matched the I_2-II-IV-VI_4 reference patterns, as shown in Figures 3.14 and 3.15.

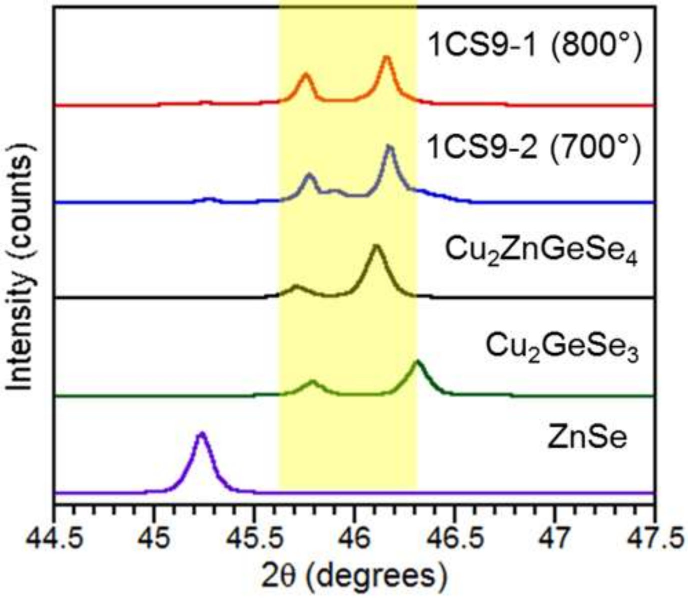

Figure 3.12. XRPD patterns (top) intended to prepare $Cu_2ZnGeSe_4$ at 700 °C and 800 °C for 4 days compared to the $Cu_2ZnGeSe_4$ reference pattern[88] and the reference patterns of frequently encountered secondary phases, Cu_2GeSe_3[100] and ZnSe.[101]

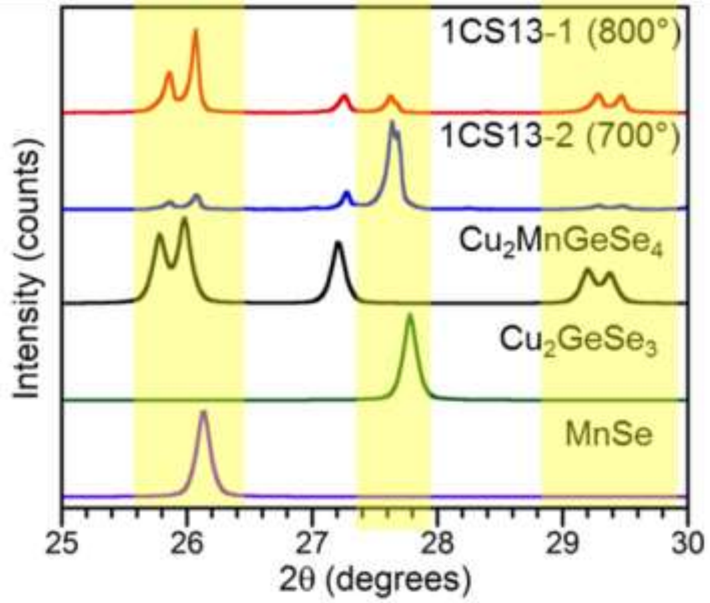

Figure 3.13. XRPD patterns (top) intended to prepare $Cu_2MnGeSe_4$ at 700 °C and 800 °C for 4 days compared to the $Cu_2MnGeSe_4$ reference pattern[32] and the reference patterns of frequently encountered secondary phases, Cu_2GeSe_3[100] and MnSe.[102]

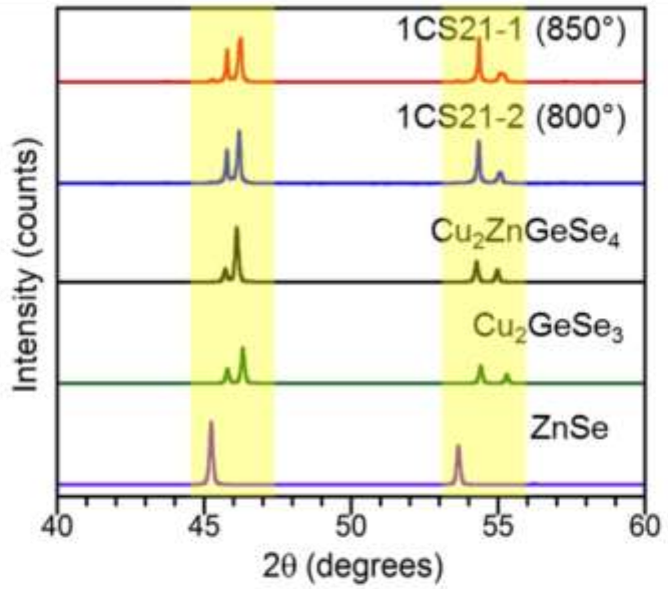

Figure 3.14. XRPD patterns (top) intended to prepare $Cu_2ZnGeSe_4$ at 850 °C and 800 °C for 8 days compared to the $Cu_2ZnGeSe_4$ reference pattern[88] and the reference patterns of frequently encountered secondary phases, Cu_2GeSe_3[100] and ZnSe.[101]

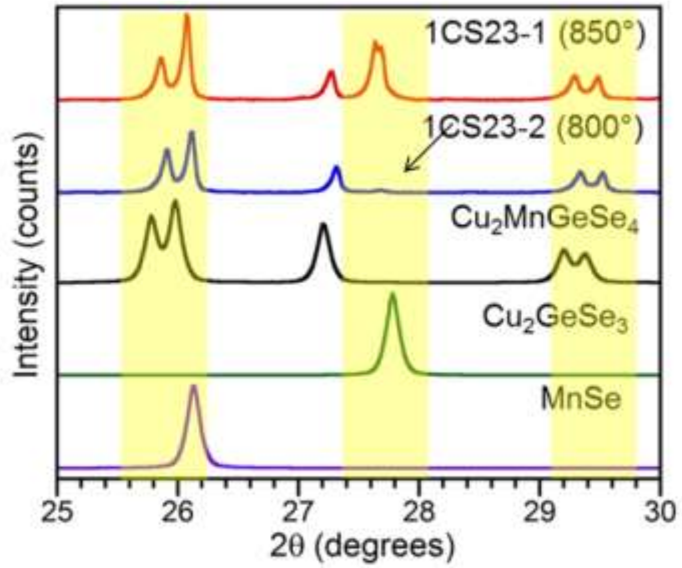

Figure 3.15. XRPD patterns (top) intended to prepare $Cu_2MnGeSe_4$ at 850 °C and 800 °C for 8 days compared to the $Cu_2MnGeSe_4$ reference pattern[32] and the reference patterns of frequently encountered secondary phases, Cu_2GeSe_3[100] and MnSe.[102]

Even though these heating profiles yielded products that were *nearly* phase pure, minor technique adjustments were made to try and reach "*complete*" phase purity. Three minor synthesis adjustments were implemented: 1) no grinding of the elemental starting materials, 2) the addition of 5 % excess selenium to maintain stoichiometry and to reduce the formation of vacancies in the structure,[34] and 3) doubling of the reaction to reduce the significance of the errors in measuring the masses of starting materials. Both $Cu_2ZnGeSe_4$ and $Cu_2MnGeSe_4$ were synthesized employing these adjustments, each adjustment individually and then a reaction employing a combination of all three. After XRPD analysis, it was determined that all of these adjustments improved phase-purity, especially the addition of 5 % excess selenium. Small impurity peaks were eliminated (Figures 3.16) and sharper intensity of peaks which better matched the reference patterns, were observed (Figures 3.17 and 3.18).

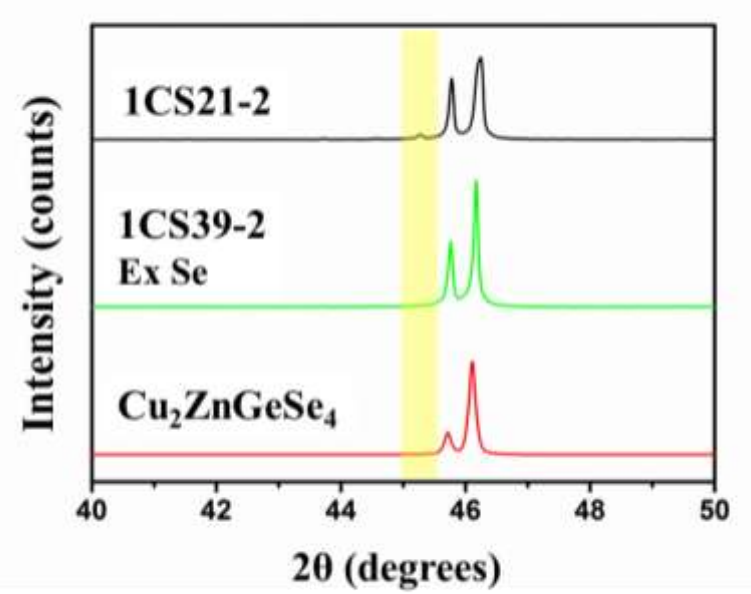

Figure 3.16. XRPD pattern intended to prepare $Cu_2ZnGeSe_4$ at 800 °C for 8 days using excess Se (green) better matches the $Cu_2ZnGeSe_4$ reference pattern88 (red) when compared to the XRPD pattern with no synthesis technique adjustments (black) as small impurity peaks are eliminated.

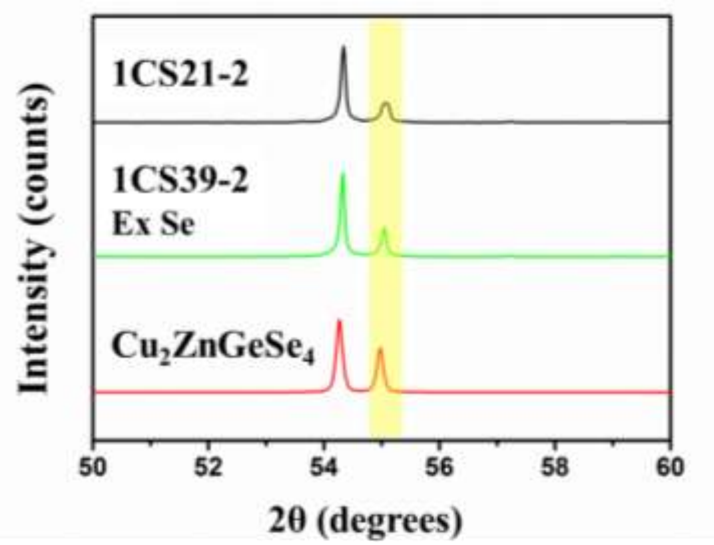

Figure 3.17. XRPD pattern intended to prepare $Cu_2ZnGeSe_4$ at 800 °C for 8 days using excess Se (green) better matches the $Cu_2ZnGeSe_4$ reference pattern88 (red) when compared to the XRPD pattern with no synthesis technique adjustments (black) as peaks with sharper intensity are observed.

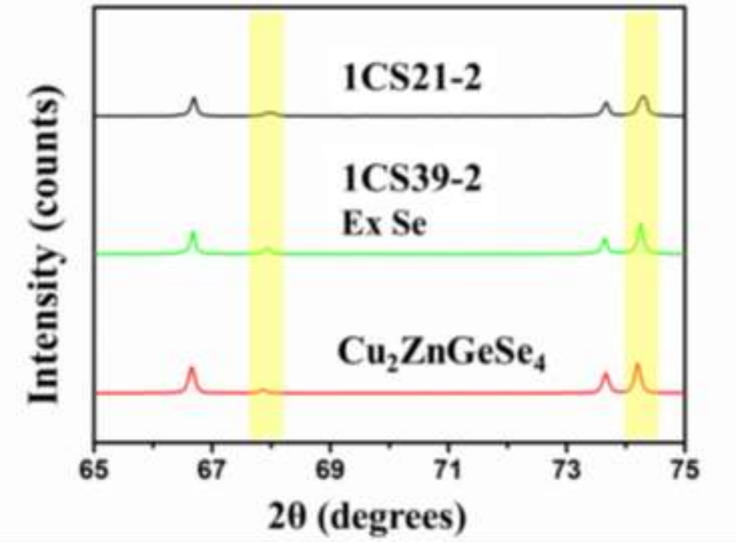

Figure 3.18. XRPD pattern intended to prepare $Cu_2ZnGeSe_4$ at 800 °C for 8 days using excess Se (green) better matches the $Cu_2ZnGeSe_4$ reference pattern88 (red) when compared to the XRPD pattern with no synthesis technique adjustments (black) as peaks with sharper intensity are observed.

Throughout this quest to prepare $Cu_2ZnGeSe_4$ phase pure, a new compound $Cu_4ZnGe_2Se_7$ was serendipitously discovered. This new compound was first found in a reaction that was heated to 700 °C for 4 days using the 2:1:1:4 Cu:Zn:Ge:Se stoichiometry. After solving and refining the single crystal structure, as described previously, a simulated reference XRPD pattern for the new $Cu_4ZnGe_2Se_7$ compound was generated and compared to the pattern for $Cu_2ZnGeSe_4$, see Figures 3.19 and 3.20. While the X-ray powder diffraction patterns for $Cu_4ZnGe_2Se_7$ and $Cu_2ZnGeSe_4$ are quite similar, there are a few regions of the pattern that can be used to differentiate the two phases. In the regions of ~ 55°, 65°, and 75° 2θ, there are two peaks in the $Cu_2ZnGeSe_4$ reference pattern, while there are 3 peaks for the $Cu_4ZnGe_2Se_7$ reference pattern. The X-ray powder diffraction pattern of the product intended to prepare $Cu_2ZnGeSe_4$ at 800 °C clearly shows 2 peaks and best matches the calculated pattern for $Cu_2ZnGeSe_4$. However, the X-ray powder diffraction pattern of the reaction product heated to only 700 °C displays sets of 3 peaks that better match the calculated pattern for $Cu_4ZnGe_2Se_7$.

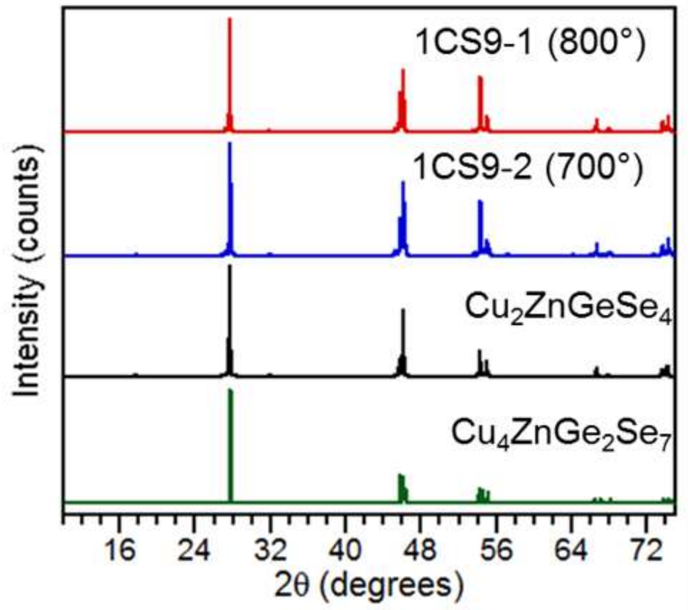

Figure 3.19. The entire XRPD pattern (top) intended to prepare $Cu_2ZnGeSe_4$ at 700 °C and 800 °C for 4 days compared to the $Cu_2ZnGeSe_4$ reference pattern[88] and the reference pattern of $Cu_4ZnGe_2Se_7$ that look very similar.

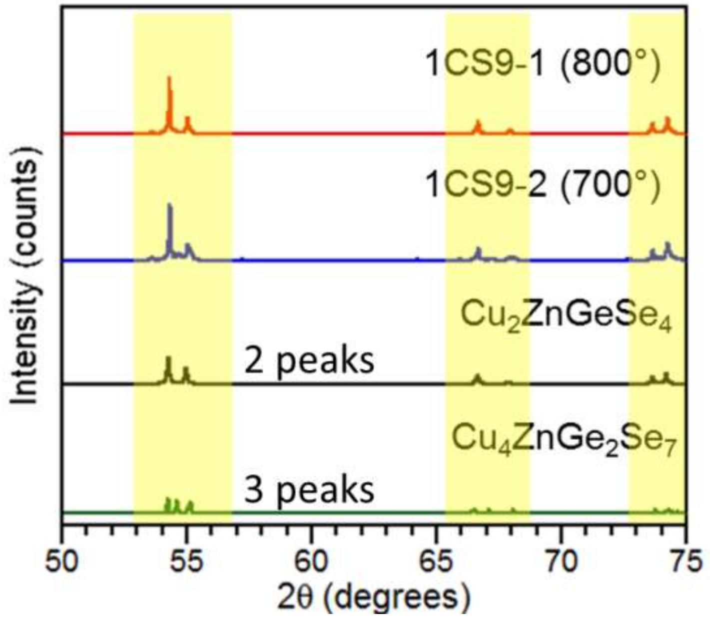

Figure 3.20. XRPD patterns (top) intended to prepare $Cu_2ZnGeSe_4$ at 700 °C and 800 °C for 4 days compared to the $Cu_2ZnGeSe_4$ reference pattern[88] and the reference pattern of $Cu_4ZnGe_2Se_7$ from 50° 2θ to 75° 2θ.

Synthesis of $Cu_4ZnGe_2Se_7$ using the actual 4:1:2:7 stoichiometry of elemental reagents was carried out using different heating profiles with maximum temperatures ranging from 700 °C to 850 °C and hold times of 4 and 8 days. After close inspection of the XRPD patterns, it could be seen that $Cu_4ZnGe_2Se_7$ was synthesized almost phase pure at 800 °C for 4 days (Figures 3.21 and 3.22). All peaks in the collected pattern could be indexed to the $Cu_4ZnGe_2Se_7$ phase.

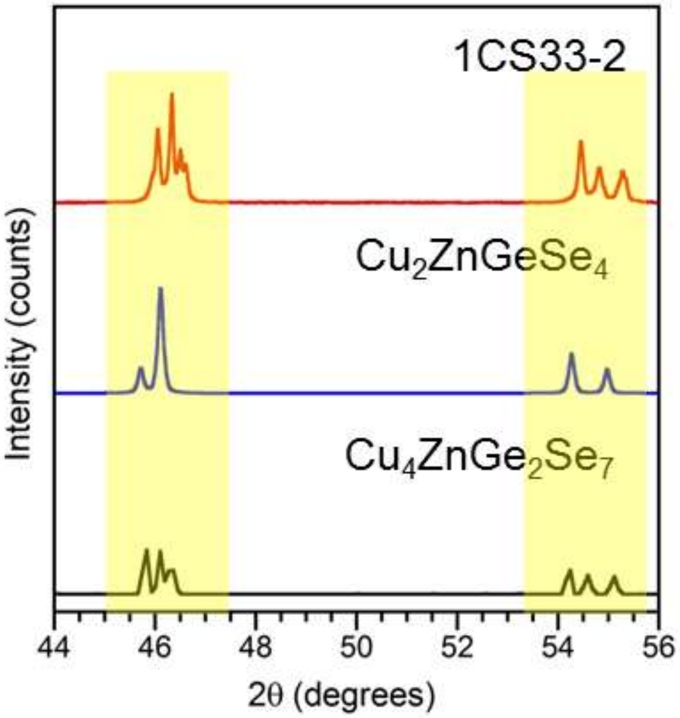

Figure 3.21. XRPD pattern (top) intended to prepare $Cu_4ZnGe_2Se_7$ at 800 °C for 4 days compared to the $Cu_2ZnGeSe_4$ reference pattern[88] and the reference pattern of $Cu_4ZnGe_2Se_7$ from 44° 2θ to 56° 2θ showing how close the experimental data matches the $Cu_4ZnGe_2Se_7$ reference pattern with sets of 3 peaks instead of 2.

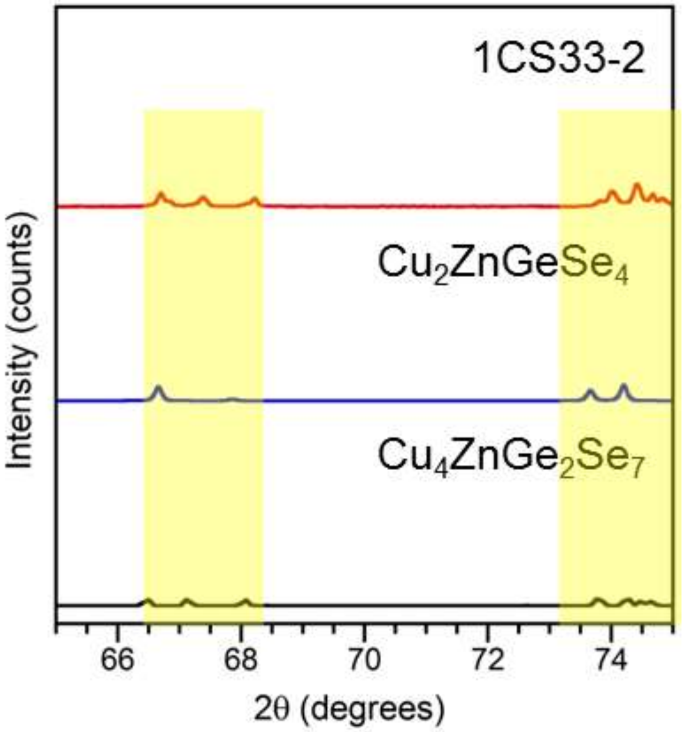

Figure 3.22. XRPD pattern (top) intended to prepare $Cu_4ZnGe_2Se_7$ at 800 °C for 4 days compared to the $Cu_2ZnGeSe_4$ reference pattern[88] and the reference pattern of $Cu_4ZnGe_2Se_7$ from 66° 2θ to 74° 2θ showing how close the experimental data matches the $Cu_4ZnGe_2Se_7$ reference pattern with sets of 3 peaks instead of 2.

Although these heating profiles provided products that were nearly phase pure, there appeared to be some very minor shoulders on some of the reflections indicating that there may be the presence of both phases in the samples. Therefore, reactions using "the three minor synthesis adjustments" including no grinding, excess selenium, and doubling of the reaction were again carried out. Just as in the case of $Cu_2ZnGeSe_4$, these minor technique adjustments seemed to improve the phase purity of the product, especially the reaction carried out with no grinding (Figure 3.23). A closer inspection of the XRPD pattern shows that this synthesis technique may have eliminated any $Cu_2ZnGeSe_4$ in the product, as seen in Figure 3.24. However, in order to more definitely assess phase purity synchrotron X-ray powder diffraction was employed.

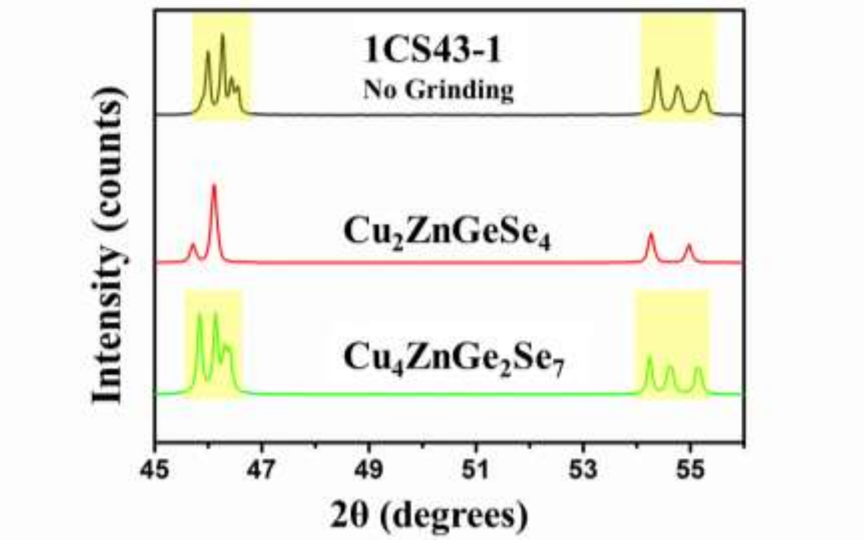

Figure 3.23. XRPD pattern intended to prepare $Cu_4ZnGe_2Se_7$ at 800 °C for 8 days with no grinding (black) compared to the $Cu_2ZnGeSe_4$ reference pattern[88] (red) and the reference pattern of $Cu_4ZnGe_2Se_7$ (green).

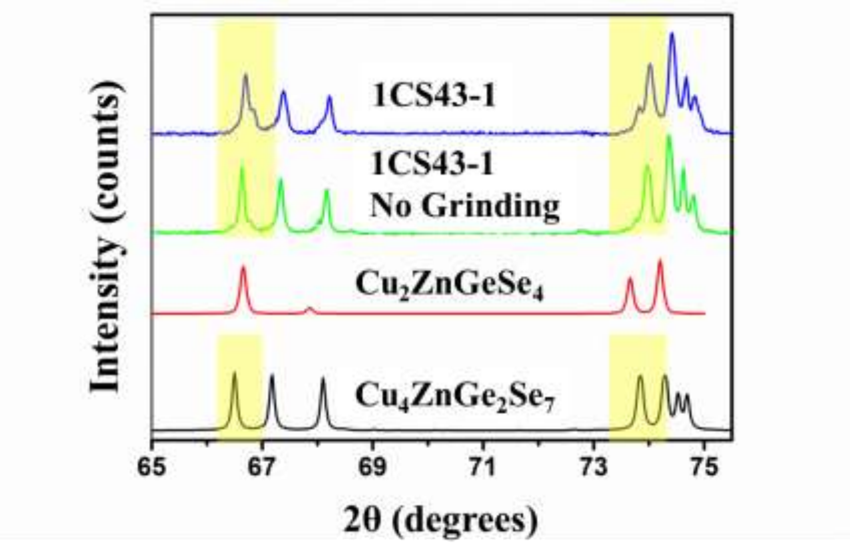

Figure 3.24. XRPD pattern intended to prepare $Cu_4ZnGe_2Se_7$ at 800 °C for 8 days with no grinding (black) compared to the XRPD pattern with no synthesis technique adjustments (blue) shows small impurity peaks, possibly excess $Cu_2ZnGeSe_4$, are eliminated when compared to the $Cu_2ZnGeSe_4$ reference pattern[88] and the reference pattern of $Cu_4ZnGe_2Se_7$.

3.2.3 High-Resolution Synchrotron X-ray Powder Diffraction (SXRPD) and Rietveld Refinements

The X-ray powder diffraction patterns for many of the quaternary DLS structures along with possible binary and ternary impurities are strikingly similar and difficult to distinguish with the use of laboratory-grade X-ray powder diffraction. Therefore, samples of $Cu_2ZnGeSe_4$ and $Cu_4ZnGe_2Se_7$ were sent out for high-resolution synchrotron XRPD to better evaluate phase-purity. Rietveld refinement using the synchrotron data and the previously reported structure of $Cu_2ZnGeSe_4$[88] as the starting model resulted in suitable refinement statistics, $\chi^2 = 4.380$, $R_p = 0.1424$ and $R_{wp} = 0.1716$. The Rietveld refinement results for $Cu_2ZnGeSe_4$ are shown in Figure 3.25. Refined atomic coordinates, as well as bond distances and angles are displayed in Tables 3.6 and 3.7, respectively.

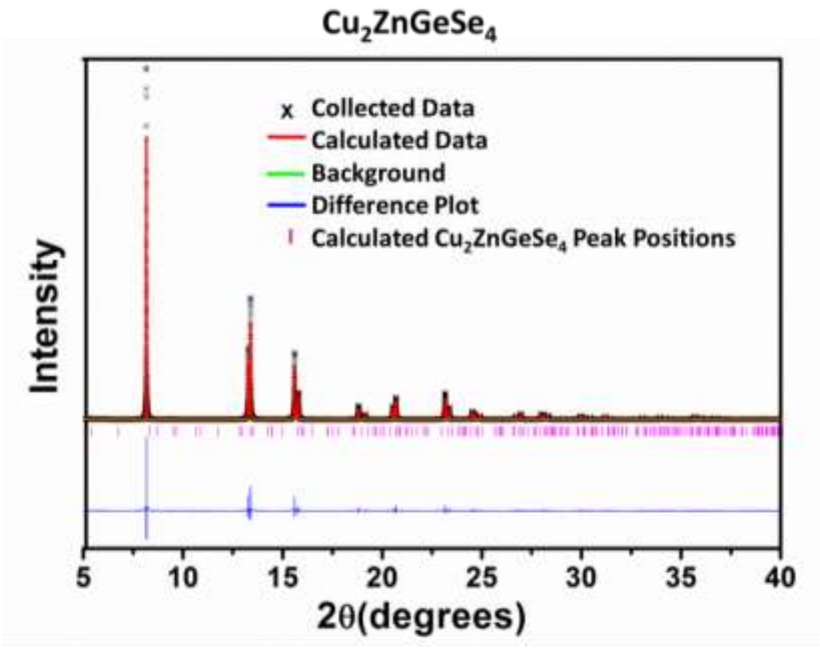

Figure 3.25. Rietveld refinement results for $Cu_2ZnGeSe_4$ using SXRPD data plotted with x markers representing collected data, nearly overlapped by the pattern calculated from the model (red line). Expected Bragg reflections for the $Cu_2ZnGeSe_4$ phase are displayed with tick marks (|). The difference between the observed data and the calculated pattern is shown at the bottom of the plot (blue line).

Table 3.6. Atomic coordinates and isotropic displacement parameters (U_{iso}) from Rietveld refinement of $Cu_2ZnGeSe_4$ using SXRPD data.

Site	Multiplicity Wyckoff Letter	x	y	z	U_{iso} Å^2
Cu1	4d	0.500000	0.000000	0.250000	0.010375(2)
Zn1	2a	0.000000	0.000000	0.000000	0.024876(2)
Ge1	2b	0.000000	0.000000	0.500000	0.018673(2)
Se1	8i	0.256289(2)	0.256289(3)	0.126630(2)	0.011961(2)

Table 3.7. Bond distances (Å) and angles (°) from Rietveld refinement of $Cu_2ZnGeSe_4$ using SXRPD data.

Cu1—Se1 (x4)	2.40910(1)	Se1—Cu1—Se1 (x2)	111.093(1)
Zn1—Se1 (x4)	2.47015(1)	Se1—Cu1—Se1 (x4)	108.667(2)
Ge1—Se1 (x4)	2.38848(2)	Se1—Zn1—Se1 (x2)	111.010(1)
Cu1—Se1—Ge1 (x2)	110.375(1)	Se1—Zn1—Se1 (x4)	108.707(1)
Cu1—Se1—Cu1	111.040(1)	Se1—Ge1—Se1 (x2)	108.295(3)
Cu1—Se1—Zn1 (x2)	107.656(2)	Se1—Ge1—Se1 (x4)	110.063(1)
Zn1—Se1—Ge1	109.652(1)		

Powdered samples of $Cu_4ZnGe_2Se_7$ were sent to Argonne National Laboratory for high-resolution synchrotron XRPD and Rietveld refinement was again carried out to better assess the phase purity. The starting model for $Cu_4ZnGe_2Se_7$ was obtained from the single crystal structure solution previously described in Chapter 2. $Cu_2ZnGeSe_4$ was added as a secondary phase in order to better fit the diffraction pattern. When the $Cu_2ZnGeSe_4$ phase was added to the Rietveld refinement model, the phase fraction refined to 5 wt. %. Rietveld refinements indicate that the $Cu_4ZnGe_2Se_7$ sample has been synthesized with > 95 wt. % phase purity with agreeable refinement statistics of $\chi^2 = 3.464$, $R_p = 0.1145$ and $R_{wp} = 0.0958$ as shown in Figure 3.26. Refined atomic coordinates, as well as bond lengths and angles are displayed in Tables 3.8 and 3.9 and are in close agreement with those obtained from single crystal X-ray diffraction. These results confirm the previously reported *I*-42*m* structure of $Cu_2ZnGeSe_4$ and the new structure of $Cu_4ZnGe_2Se_7$, which crystallizes in the *C*2 space group.

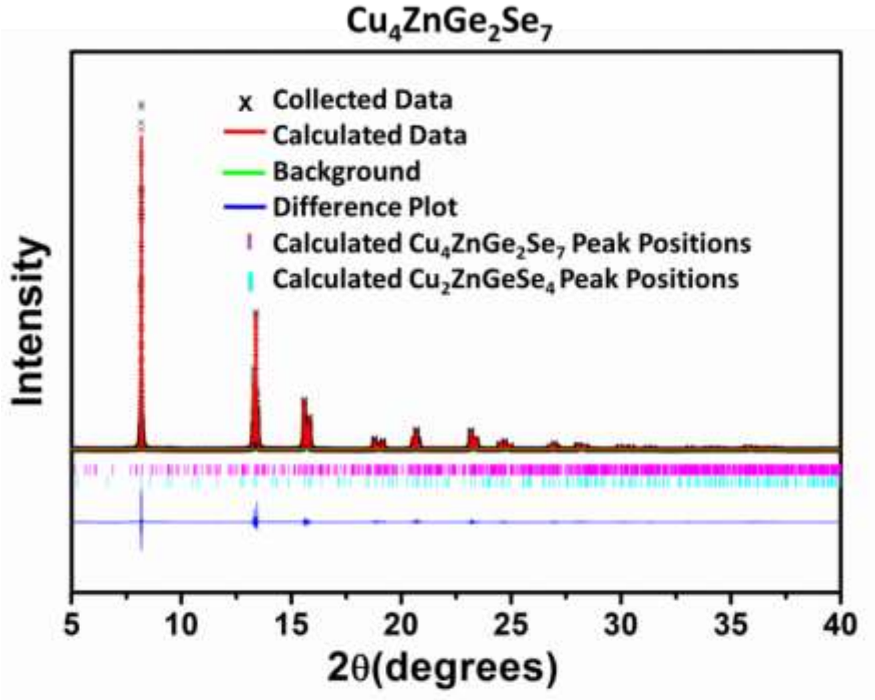

Figure 3.26. Rietveld refinement of the $Cu_4ZnGe_2Se_7$ structure model using SXRPD data with x markers representing collected data, nearly overlapped by the calculated pattern using the model (red line). Expected Bragg reflections $Cu_4ZnGe_2Se_7$ and $Cu_2ZnGeSe_4$ are designated with tick marks (|) from top to bottom, respectively. The difference between the collected data and the pattern calculated from the model is shown at the bottom of the plot (blue line).

Table 3.8. Atomic coordinates and isotropic displacement parameters (U_{iso}) values from Rietveld refinement of $Cu_4ZnGe_2Se_7$ using SXRPD data.

Site	**Multiplicity Wyckoff Letter**	**x**	**y**	**z**	**U_{iso} Å^2**
Cu1	4c	0.1421(4)	0.0143(8)	0.4417(7)	0.01581(3)
Cu2	4c	0.2071(3)	0.5121(7)	0.1391(6)	0.00576(2)
Zn1	2a	0.0000(0)	0.0000(0)	0.0000(0)	0.03097(2)
Ge1	4c	0.4252(3)	0.9845(6)	0.2815(6)	0.01849(2)
Se1	2b	0.0000(0)	0.7460(8)	0.5000(0)	0.01271(3)
Se2	4c	0.0725(2)	0.2567(6)	0.2188(5)	0.01351(2)
Se3	4c	0.2842(2)	0.7584(6)	0.3605(4)	0.00511(2)
Se4	4c	0.3597(2)	0.2615(6)	0.0779(6)	0.01311(3)

Table 3.9. Bond distances (Å) and angles (°) from Rietveld refinement of $Cu_4ZnGe_2Se_7$ using SXRPD data.

Cu1—Se3$^{\mathrm{i}}$	2.296(6)	Se3$^{\mathrm{i}}$—Cu1—Se2	109.1(2)
Cu1—Se2	2.438(5)	Se3$^{\mathrm{i}}$—Cu1—Se3$^{\mathrm{ii}}$	110.5(2)
Cu1—Se3$^{\mathrm{ii}}$	2.460(5)	Se2—Cu1—Se3$^{\mathrm{ii}}$	105.9(2)
Cu1—Se1	2.430(5)	Se3$^{\mathrm{i}}$—Cu1—Se1	115.3(2)
		Se2—Cu1—Se1	109.8(2)
		Se3$^{\mathrm{ii}}$—Cu1—Se1	105.6(2)
Cu2—Se2	2.384(5)	Se2—Cu2—Se3	108.0(2)
Cu2—Se3	2.463(7)	Se2—Cu2—Se4	108.0(1)
Cu2—Se4	2.414(6)	Se3—Cu2—Se4	106.0(2)
Cu2—Se4$^{\mathrm{iii}}$	2.479(5)	Se2—Cu2—Se4$^{\mathrm{iii}}$	114.3(2)
		Se3—Cu2—Se4$^{\mathrm{iii}}$	110.1(2)
		Se4—Cu2—Se4$^{\mathrm{iii}}$	109.8(2)
Zn1—Se2$^{\mathrm{iv}}$	2.466(5)	Se2$^{\mathrm{iv}}$—Zn1—Se2	108.2(3)
Zn1—Se2	2.466(5)	Se2$^{\mathrm{iv}}$—Zn1—Se4$^{\mathrm{v}}$	111.1(1)
Zn1—Se4$^{\mathrm{v}}$	2.374(4)	Se2—Zn1—Se4$^{\mathrm{v}}$	107.5(1)
Zn1—Se4$^{\mathrm{vi}}$	2.374(4)	Se2$^{\mathrm{iv}}$—Zn1—Se4$^{\mathrm{vi}}$	107.5(1)
		Se2—Zn1—Se4$^{\mathrm{vi}}$	111.1(1)
		Se4$^{\mathrm{v}}$—Zn1—Se4$^{\mathrm{vi}}$	111.1(3)
Ge1—Se3	2.347(5)	Se3—Ge1—Se2$^{\mathrm{vii}}$	114.1(2)
Ge1—Se2$^{\mathrm{vii}}$	2.360(6)	Se3—Ge1—Se4$^{\mathrm{viii}}$	112.8(2)
Ge1—Se4$^{\mathrm{viii}}$	2.421(5)	Se2$^{\mathrm{vii}}$—Ge1—Se4$^{\mathrm{viii}}$	111.1(2)
Ge1—Se1$^{\mathrm{ix}}$	2.487(5)	Se3—Ge1—Se1$^{\mathrm{ix}}$	107.3(2)
		Se2$^{\mathrm{vii}}$—Ge1—Se1$^{\mathrm{ix}}$	107.0(2)
		Se4$^{\mathrm{viii}}$—Ge1—Se1$^{\mathrm{ix}}$	103.6(2)

Symmetry codes: (i) −*x*+1/2, *y*−1/2, −*z*+1; (ii) *x*, *y*−1, *z*; (iii) −*x*+1/2, *y*+1/2, −*z*; (iv) −*x*, *y*, −*z*; (v) *x*−1/2, *y*−1/2, *z*; (vi) −*x*+1/2, *y*−1/2, −*z*; (vii) *x*+1/2, *y*+1/2, *z*; (viii) *x*, *y*+1, *z*; (ix) *x*+1/2, *y*+3/2, *z*.

3.2.4 Scanning Electron Microscopy and Energy Dispersive Spectroscopy (SEM/EDS)

Energy dispersive spectroscopy (EDS), which is a semi-quantitative elemental analysis, was performed to determine the elemental ratio of the I_2-II-IV-VI_4 compounds and $Cu_4ZnGe_2Se_7$. The compositions were found to be $Cu_{2.1(2)}Mn_{1.0(1)}Ge_{1.1(1)}Se_{3.9(4)}$, $Cu_{2.1(1)}Zn_{1.0(1)}Ge_{1.1(2)}Se_{4.2(3)}$, and $Cu_{4.1(2)}Zn_{1.0(1)}Ge_{2.1(1)}Se_{7.1(3)}$, which are close to the intended compositions. This further confirmed the synthesis of the target compounds as the results relatively matched the intended 2:1:1:4 and 4:1:2:7 elemental ratios respectively.

3.2.5 Inductively Coupled Plasma Optical Emission Spectroscopy (ICP-OES)

Inductively coupled plasma optical emission spectroscopy (ICP-OES) was performed on samples of $Cu_2ZnGeSe_4$ and $Cu_4ZnGe_2Se_7$, in addition to EDS, to confirm the intended ratio of elements within the products. Accordingly, stoichiometries of $Cu_{2.0}Zn_{1.0}Ge_{1.1}Se_{3.9}$ and $Cu_{3.9}Zn_{1.0}Ge_{2.2}Se_{6.8}$ were observed.

3.2.6 Optical Diffuse Reflectance UV/Vis/NIR Spectroscopy

Optical diffuse reflectance spectra of the $Cu_2ZnGeSe_4$ and the $Cu_4ZnGe_2Se_7$ compounds were collected over the ultraviolet, visible, and near infrared spectral regimes (UV/Vis/NIR). Upon examination of the spectra for $Cu_2ZnGeSe_4$, a relatively sharp absorption edge at ~ 1.3 eV can be observed that closely matches the values reported in the literature (~ 1.5 eV).[37,103]

For the $Cu_4ZnGe_2Se_7$ compound, the absorption edge is found at a lower energy, ~ 1.0 eV. A comparison of the bandgaps for $Cu_2ZnGeSe_4$ and $Cu_4ZnGe_2Se_7$ are shown in

Figure 3.27. If converted from eV to nm, values of 953.72 nm and 1239.84 nm are found for the bandgaps of $Cu_2ZnGeSe_4$ and $Cu_4ZnGe_2Se_7$ respectively, in the NIR region.

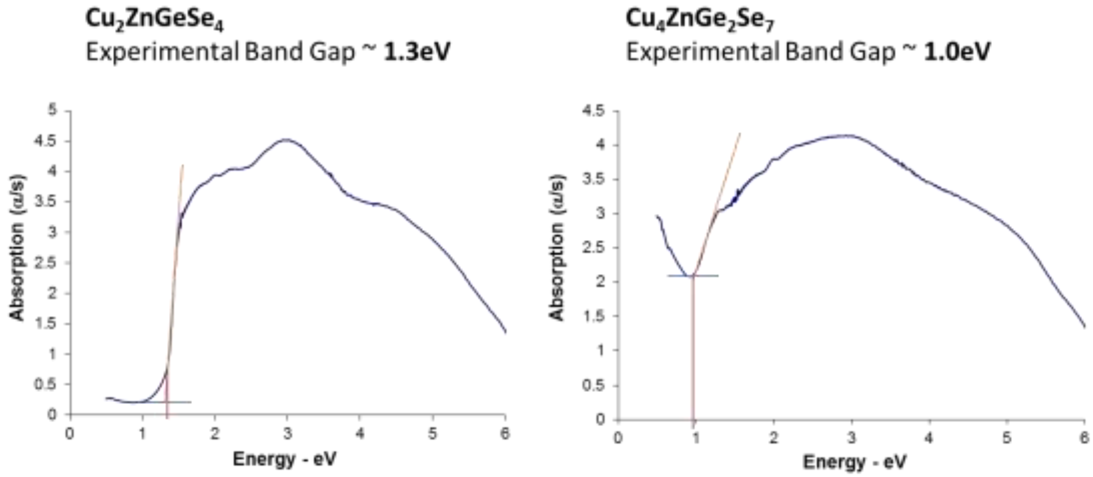
$Cu_2ZnGeSe_4$
Experimental Band Gap ~ **1.3eV**

$Cu_4ZnGe_2Se_7$
Experimental Band Gap ~ **1.0eV**

Figure 3.27. Absorption edges of $Cu_2ZnGeSe_4$ (left) and $Cu_4ZnGe_2Se_7$ (right) corresponding to bandgaps of approximately 1.3 eV and 1.0 eV, respectively.

It must be taken into account that optical absorption edges may commonly exhibit a diffuse tail that originates from defects within the crystal structure that will cause defect states within the band structure. These defect states occur at the top of the valence and the bottom of the conduction bands, creating a smearing of the band edge known as the Urbach tail, which can be clearly seen at energies just below the band gap.[104,105] This tail should be considered when analyzing the bandgap of a semiconductor, as it provides a lower bound for the bandgap energy.[106] The Urbach tail appears as a linear region when the logarithm of the absorption is plotted against the incident photon energy.

In semiconductor materials, a relatively sharp absorption edge is indicative of a direct bandgap material, while a more gradual onset designates a bandgap of indirect character.[107] To determine the nature of the bandgap, the absorption data, excluding the previously found Urbach tail region, were fitted to the function for a direct gap semiconductor, $\alpha = A\bullet(E-E_g)^{1/2}/E$, and to the function for an indirect semiconductor, $\alpha = A\bullet(E-E_g)^2/E$, where A is a constant, E is the photon energy in eV, and E_g is the bandgap energy.[90] Both the square of the absorption and the square root of the absorption were plotted as a function of energy and the data were fitted to the indirect and direct functions, respectively. It was found that the fitted data of both $Cu_2ZnGeSe_4$ and $Cu_4ZnGe_2Se_7$ exhibited a larger range of linearity using the direct function rather than the indirect function, and thus both compounds were determined to have direct bandgaps. Therefore, optical bandgaps of 1.38 eV and 0.91 eV were determined for $Cu_2ZnGeSe_4$ and $Cu_4ZnGe_2Se_7$, respectively using the direct-gap functional form.[108] These bandgaps agree well with the dark color of the samples. The optical diffuse reflectance spectra of both materials including the fitting of the Urbach tail are shown in Figure 3.28. These results are significant because $Cu_2ZnGeSe_4$ is growing in interest for solar cells due to its bandgap being close to the ideal value for solar cells (~1.4 eV) and if $Cu_4ZnGe_2Se_7$ is actually synthesized rather than $Cu_2ZnGeSe_4$ then there will be a lower bandgap. Even though this lower bandgap may not be advantageous for absorber layers in solar cells, it may make the compound more attractive for thermoelectric applications with an expected increase in electrical conductivity. This lower bandgap may also make the compound more attractive for NLO applications due to a suspected higher second-order nonlinear optical susceptibility ($\chi^{(2)}$). In order to better understand the origin of the bandgap in these two compounds, electronic structure calculations were carried out.

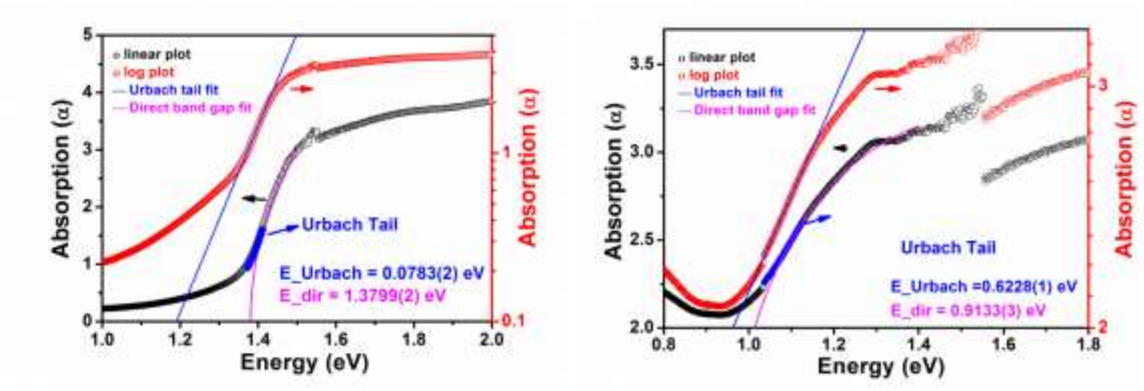

Figure 3.28. Optical diffuse reflectance spectra of $Cu_2ZnGeSe_4$ (left) and $Cu_4ZnGe_2Se_7$ (right) with both linear and log scales. The data were fit using Tauc's function for direct-gap semiconductors, while the Urbach tail region was excluded from the region used for fitting.

3.2.7 Attenuated Total Reflectance (ATR) FT-IR Spectroscopy

ATR FT-IR spectroscopy was used to assess the windows of optical clarity for $Cu_2ZnGeSe_4$ and $Cu_4ZnGe_2Se_7$. Both of these DLSs exhibit optical transparency into the far IR. In fact, their transparency seems to extend beyond the detection limit of FT-IR (25 μm), indicating great potential for NLO applications.

As shown in Figure 3.29, $Cu_2ZnGeSe_4$ absorbs radiation in the NIR region due to its bandgap of 1.38 eV and the transparency region has a lower limit of ~1 μm. Similarly, $Cu_4ZnGe_2Se_7$ exhibits bandgap absorption of 0.91 eV in the NIR region. $Cu_2ZnGeSe_4$ has a window of optical transparency > 70 % from ~1.0 μm to 25 μm, whereas $Cu_4ZnGe_2Se_7$ shows lower transparency in the Vis/NIR range. However, in the IR and far IR range $Cu_4ZnGe_2Se_7$ shows a similar transparency to $Cu_2ZnGeSe_4$

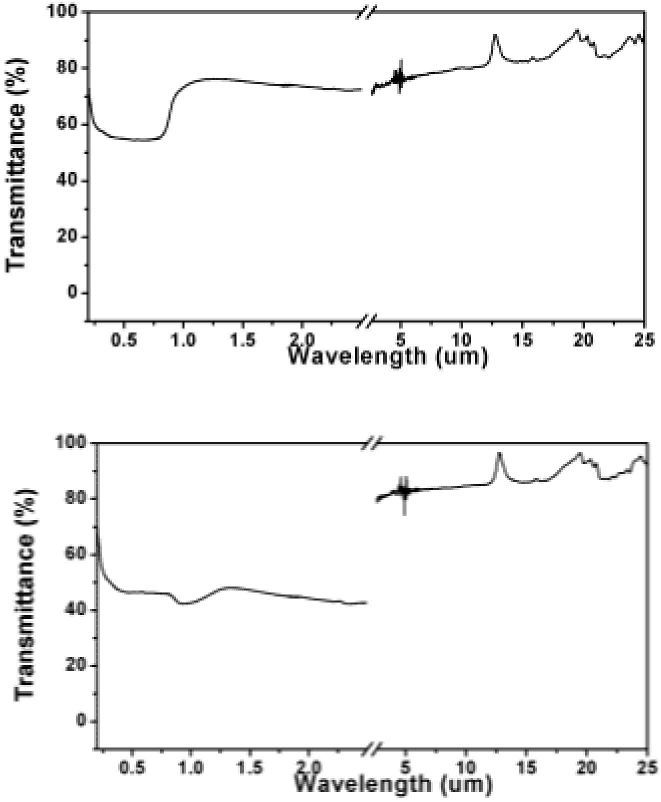

Figure 3.29. Optical transparency windows of $Cu_2ZnGeSe_4$ (top) and $Cu_4ZnGe_2Se_7$ (bottom) in UV-vis-NIR and IR regions.

3.2.8 Differential Thermal Analysis (DTA)

Two cycles of DTA data were collected for both $Cu_2ZnGeSe_4$ and $Cu_4ZnGe_2Se_7$. As shown in Figure 3.30, upon heating an endothermic peak for $Cu_2ZnGeSe_4$ appears at 892 °C for both cycles, and upon cooling the exothermic peaks occur at 876 and 794 °C, respectively. The peaks at 892 °C and 876 °C were identified as the melting and recrystallization points, respectively. Whereas the other exothermic peak at 794 °C may be caused by a possible solid-to-solid phase transition.

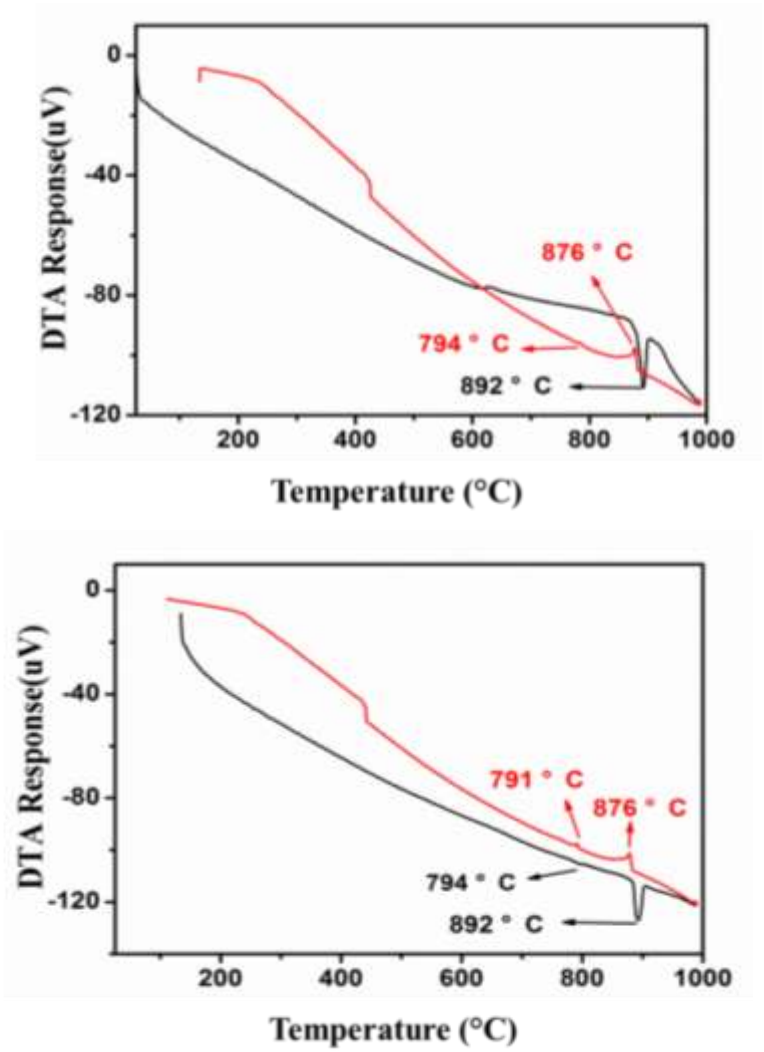

Figure 3.30. Differential thermal analysis diagrams of the first (top) and second (bottom) heating/cooling cycles for $Cu_2ZnGeSe_4$. The black and red lines indicate the heating and cooling cycles, respectively.

$Cu_4ZnGe_2Se_7$ seems to have similar melting and recrystallization points to those of $Cu_2ZnGeSe_4$. In both cycles the major endothermic peak during heating is at 887 °C and the exothermic peak during cooling is at 873 °C (Figure 3.31). However, in both cycles additional endothermic and exothermic peaks are found at 780 °C and 773 °C, respectively. This may be caused by a solid-to-solid phase transition similar to that found in the $Cu_2ZnGeSe_4$ thermogram.

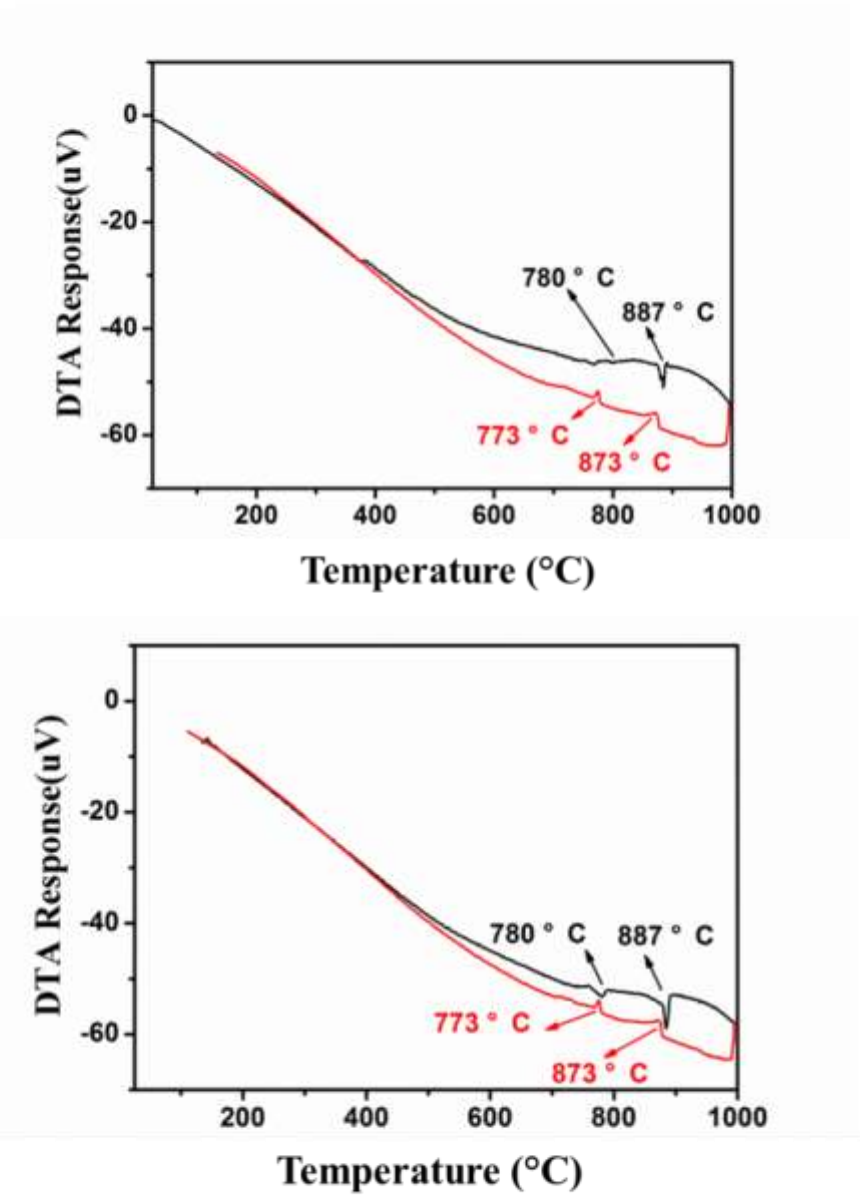

Figure 3.31. Differential thermal analysis diagrams of the first (top) and second (bottom) heating/cooling cycles for $Cu_4ZnGe_2Se_7$. The black and red lines indicate the heating and cooling curves, respectively.

3.2.9 Electronic Structure Calculations

The band structure diagram for $Cu_2ZnGeSe_4$, calculated in CASTEP, is shown in Figure 3.32. It is clear from the band structure that $Cu_2ZnGeSe_4$ is a direct bandgap semiconductor with a bandgap of 0.55 eV at the Γ-point. This calculated bandgap is a bit smaller than the experimentally determined bandgap of 1.38 eV from optical diffuse reflectance spectroscopy. However, this is to be expected since it is well established that these types of calculations tend to underestimate the bandgap due to the inability to accurately depict the exchange and correlations energy contributions. The band structure diagram for $Cu_4ZnGe_2Se_7$, also shown in Figure 3.32 and calculated in CASTEP, shows a direct bandgap of 0.41 eV at the gamma point. The fact that the calculated bandgap for $Cu_4ZnGe_2Se_7$ is narrower than that of the $Cu_2ZnGeSe_4$ agrees well with the optical absorption spectra.

In order to better understand the origin of the bandgap in these two materials and the difference in their bandgap energies we examined both the total and partial density of states. For $Cu_4ZnGe_2Se_7$, the valence band region from -9 to -7 eV principally originates from Zn-3*d*, Ge-4*s*, and Se-4*p* orbitals, with minor contributions from the Se-4*s* orbitals. Approaching the top of the valence band from -6 to -3 eV, the DOS are primarily composed of the Cu-3*d*, Ge-4*p* and Se-4*p* states, with lesser participation from the Zn-4*s*, Cu-3*s*, Cu-3*p*, and the Se-4*s* states. The states around the valance band max from -2 to 0 eV evolve predominantly from Se-4*p* and Cu-3*d* orbitals, with slight donations from the Cu-3*p*, Ge-4*p*, and Se-4*s* orbitals. On the other side of the bandgap, the minimum states in the conduction band, from +0.41 to +2 eV, chiefly arise from the Se-4*p* orbital with small donations from the Ge-4*s* and Se-4*s* orbitals. Higher in the conduction band, from +2 to +10 eV, the states are largely due to the Cu-3*p*, Ge-4*p*, Se-4*s*, and Se-4*p* orbitals along with the Zn-3*p* and Cu-4*s* orbitals.

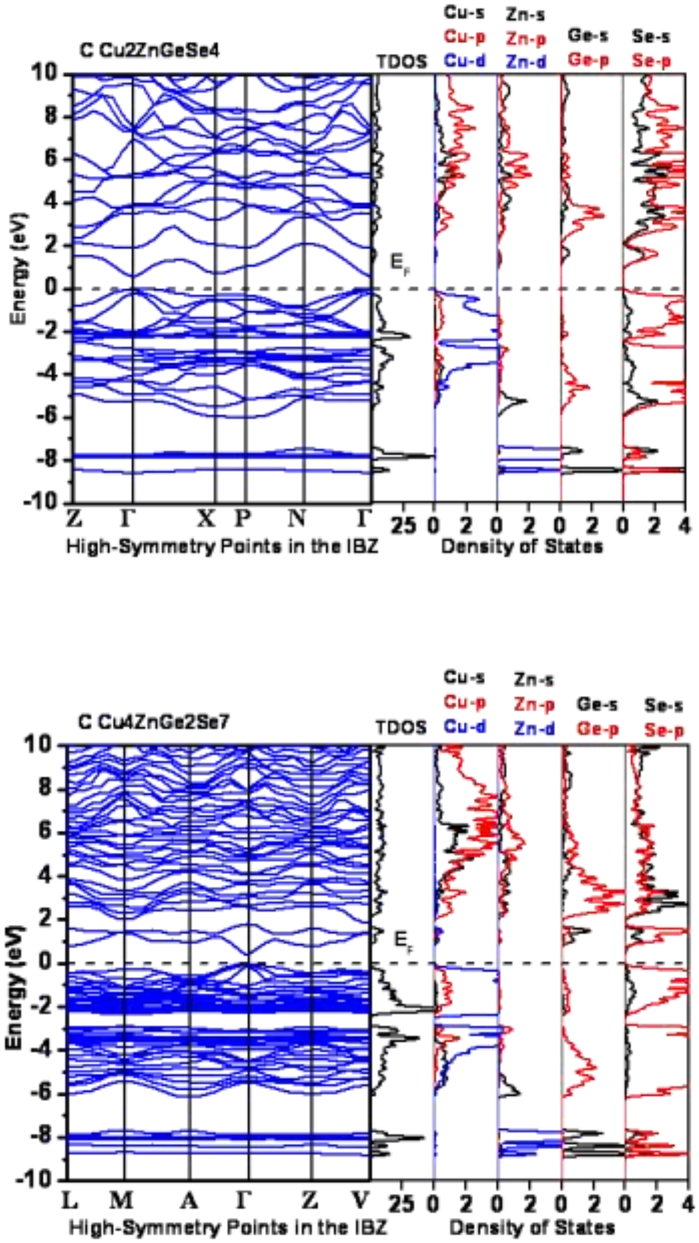

Figure 3.32. The electronic band structures (left) and the total and partial density of states (right) for $Cu_2ZnGeSe_4$ (top) and $Cu_4ZnGe_2Se_7$ (bottom).

4. Conclusion

4.1 Restatement of Purpose

The initial focus of this work was to perform an in-depth study and comparison of the crystal structure, electronic structure, and physicochemical properties of two I_2-II-IV-VI_4 diamond-like semiconductors, $Cu_2ZnGeSe_4$ and $Cu_2MnGeSe_4$. Along the way, a new compound, $Cu_4ZnGe_2Se_7$, was discovered. This led to the discovery of a new family of compounds with the structure I_4-II-IV_2-VI_7, specifically Cu_4-II-Ge_2-Se_7 where II = Mn, Fe, Co, and Ni. As described in Chapter 1, $Cu_2ZnGeSe_4$ and $Cu_2MnGeSe_4$ are known materials for which synthetic procedures, lattice parameters, and some physicochemical properties have been previously reported.[32-37] However, these materials still required more in-depth characterizations to explore their full potential for applications including nonlinear optics and thermoelectrics. The new I_4-II-IV_2-VI_7 family of compounds also needs full characterization performed as they are new compounds. The resulting physicochemical properties, along with differences in crystal and electronic structures can provide relationships between these I_2-II-IV-VI_4 and I_4-II-IV_2-VI_7 compounds, specifically $Cu_2ZnGeSe_4$ and the $Cu_4ZnGe_2Se_7$. In this conclusion chapter the major findings of this thesis will be highlighted along with potential future directions.

4.2 Importance of Proposed Activity to Advancing Knowledge and Understanding

The synthesis, characterization, and substitution of $Cu_2ZnGeSe_4$ and $Cu_2MnGeSe_4$ will provide a greater understanding of the structural and physicochemical properties of these compounds and their potential impact on applications. The synthesis and characterization of the new I_4-II-IV_2-VI_7 family of compounds provides a systematic study of compounds that have never previously been examined. $Cu_4ZnGe_2Se_7$ and $Cu_4FeGe_2Se_7$ (in appendix) are new compounds and their crystal structures have been determined. Data indicate that $Cu_4MnGe_2Se_7$, $Cu_4CoGe_2Se_7$, and $Cu_4NiGe_2Se_7$ are also new compounds that need to be synthesized phase-pure and single crystal X-ray diffraction data should be collected. The fabrication and characterization of these new compounds provides a fundamental understanding of the structure-property and composition-property relationships of this class of materials. The discovery of these new I_4-II-IV_2-VI_7 compounds will allow further research of DLSs consisting of the same elements but with different stoichiometry.

4.3 Future Work

The SHG response of these phase-powders can be determined using a modified Kurtz-NLO system. The particle size affects the SHG efficiency; therefore the samples will need to be sieved into different particle size ranges. Here, the intensity of the second harmonic in the range of 625-950nm, is collected and compared to $AgGaSe_2$ or $AgGaS_2$, two commercially-available materials. By comparing the SHG counts at the static range in which both the reference and sample are phase-matchable with minimal absorption effects, the $\chi^{(2)}$ can be estimated from the broadband data.

Thermal diffusivity measurements combined with specific heat can be used to determine the thermal conductivity of the target samples. The electrical resistivity of samples can also be measured. From the conductivity alone it is not possible to separate the number of charge carriers from their mobility, but it can be done with the combined measurements of conductivity and Hall voltage. The temperature dependence of the

Seebeck effect can also be measured and together with the electrical and thermal conductivity can be used to calculate the ZT value.

The solid solutions of the I_2-II-IV-VI_4 and I_4-II-IV_2-VI_7 materials can begin to be investigated. For the I_2-II-IV-VI_4 compounds, doping of Cu and Mn into $Cu_2ZnGeSe_4$ can be investigated to form the solid solution of $Cu_{2.1}Zn_{0.9-x}Mn_xGeSe_4$ to fine tune physical properties for applications. Since both end members have been prepared as phase-pure materials using the same heating profile, that same heating profile will be used to synthesize the solid solution. However, since the crystal structures of the two end members are different, a complete solid solution is not expected. Small values of x including 0.05, 0.10, and 0.15 can be tested but at some value of x, a change from the initial structure of $Cu_2ZnGeSe_4$ (tetragonal) to the structure of $Cu_2MnGeSe_4$ (orthorhombic) should occur. A new solid solution involving the I_4-II-IV_2-VI_7 compounds could be $Cu_4Zn_{1-x}Fe_xGe_2Se_7$, with $Cu_4FeGe_2Se_7$ being the other end members. Substitution of even more Cu into the compound, for example $Cu_{4.1}Zn_{0.9-x}Fe_xGe_2Se_7$, is also a possibility to increase the Cu-Se electrical conducting units, which will make these compounds better for thermoelectric applications.

These new I_4-II-IV_2-VI_7 compounds can be expressed as 2 I_2-IV-VI_3:II-VI, whereas the I_2-II-IV-VI_4 compounds are the 1:1 ratio of I_2-IV-VI_3:II-VI. Exploratory investigations using different ratios of I_2-IV-VI_3:II-VI, could be carried out to determine if novel compounds of new compositions can be synthesized.

This work has laid the foundation for further studies of Cu-containing I_2-II-IV-VI_4 compounds in our lab as well as enough work in the I_4-II-IV_2-VI_7 system for several Ph.D. students. The precise method of synthesis and analysis for these compounds was developed here and will lead students in the right direction to continue on this project. Furthermore, it was demonstrated how synthesis adjustments could be used to prepare phase pure materials and these modifications may be advantageous for other systems in our lab. Most importantly, rather than studying the one serendipitously discovered $Cu_4ZnGe_2Se_7$, a broad survey using a variety of transition metals as the II ion shows that this one compound was not a fluke, but rather a member of a large family of new materials.

Appendix I

The discovery of the new compound $Cu_4ZnGe_2Se_7$ warranted research into what other new compounds of this I_4-II-IV_2-VI_7 family could be prepared. To begin, compounds suspected to be isostructural to $Cu_4ZnGe_2Se_7$ were synthesized by using a different first-row transition metal that would likely adopt divalent states in the presence of selenium, Cu_4-II-Ge_2Se_7 where II = Mn, Co, Fe, and Ni. Heating profiles similar to those which were used for $Cu_4ZnGe_2Se_7$ with maximum temperatures of 700 °C and 800 °C for 4 days were initially tried. At both of these temperatures $Cu_4FeGe_2Se_7$ provided XRPD patterns with a lot of secondary phases as shown in Figure A1. The XRPD pattern of the 800 °C reaction intended to prepare $Cu_4NiGe_2Se_7$ seemed to match the 4:1:2:7 reference pattern better, but still provided secondary phases as shown in Figures A2. Even with these secondary phases present in the product, $Cu_4NiGe_2Se_7$ still has potential to be a new compound that may just need synthesis technique adjustments. $Cu_4MnGe_2Se_7$ very closely matched the 4:1:2:7 reference pattern at 800 °C when compared to the $Cu_2MnGeSe_4$ reference pattern as shown in Figure A.3. $Cu_4CoGe_2Se_7$

appeared to be synthesized phase-pure at 800 °C as the XRPD pattern very closely matched the 4:1:2:7 reference pattern; however, it also very closely matched the $Cu_2CoGeSe_4$ reference pattern (Figure A.4). Nonetheless, closer examination of the XRPD pattern around 45° 2θ shows that the experimental XRPD pattern indeed better matches the 4:1:2:7 reference pattern as shown in Figure A.5.

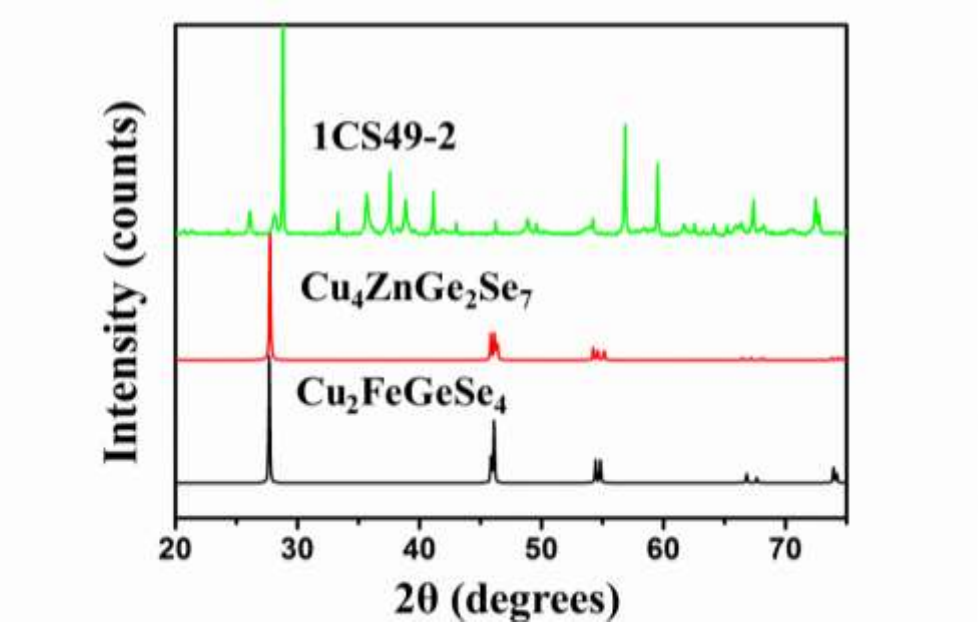

Figure A.1. XRPD pattern intended to prepare $Cu_4FeGe_2Se_7$ at 800 °C for 4 days which shows lots of secondary phases when compared to the reference pattern of $Cu_4ZnGe_2Se_7$ and $Cu_2FeGeSe_4$.

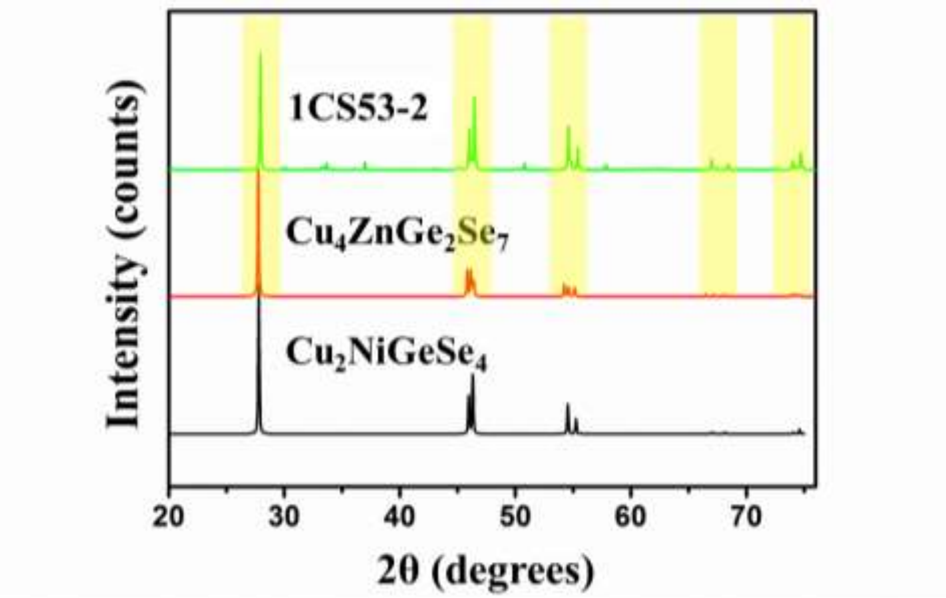

Figure A.2. XRPD pattern intended to prepare $Cu_4NiGe_2Se_7$ at 800 °C for 4 days which better matches the reference pattern of $Cu_4ZnGe_2Se_7$ when compared the $Cu_2NiGeSe_4$ reference pattern, but secondary phases are still present.

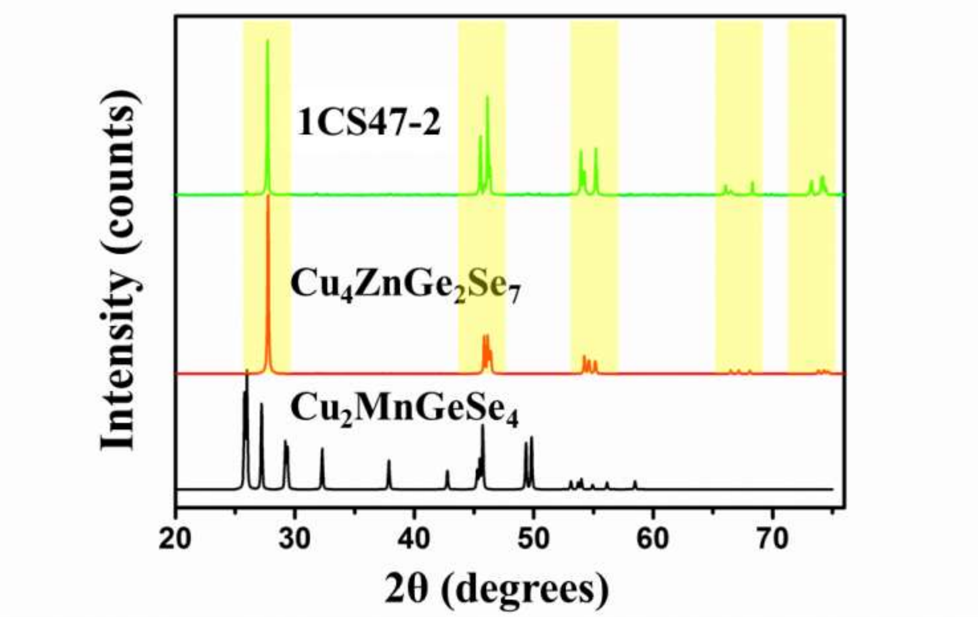

Figure A.3. XRPD pattern intended to prepare $Cu_4MnGe_2Se_7$ at 800 °C for 4 days which better matches the reference pattern of $Cu_4ZnGe_2Se_7$ when compared the $Cu_2MnGeSe_4$ reference pattern.

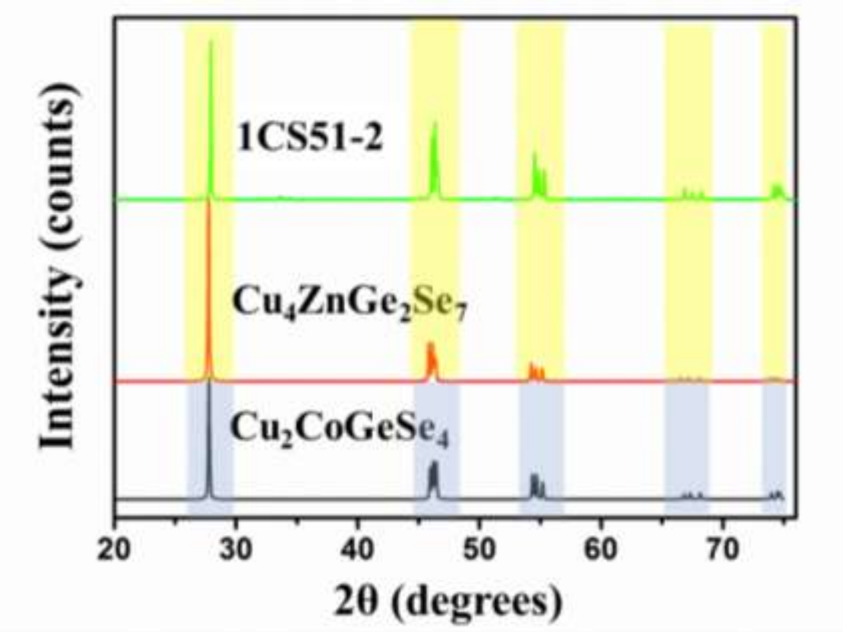

Figure A.4. XRPD pattern intended to prepare $Cu_4CoGe_2Se_7$ at 800 °C for 4 days which very closely matches the reference patterns of both $Cu_4ZnGe_2Se_7$ and $Cu_2MnGeSe_4$.

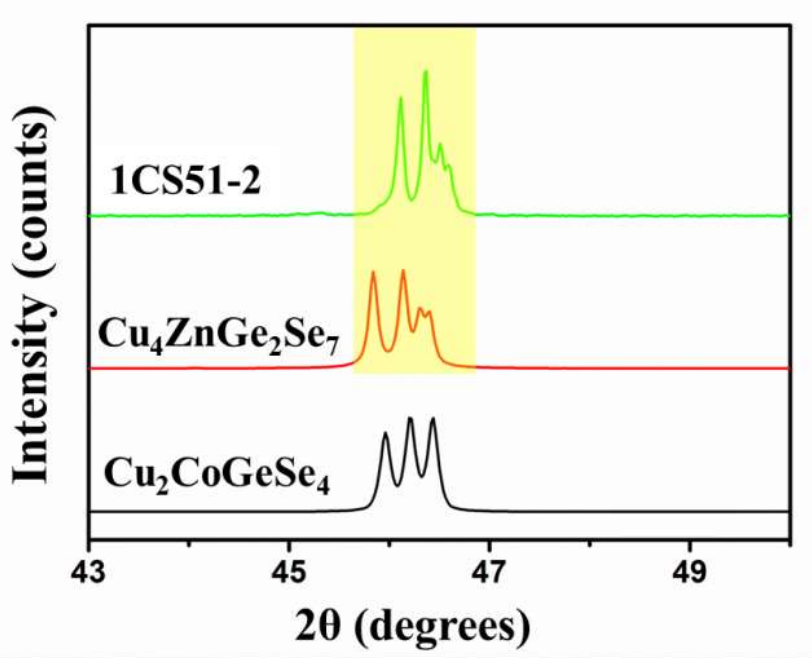

Figure A.5. Closer examination of the XRPD pattern intended to prepare $Cu_4CoGe_2Se_7$ at 800 °C for 4 days clearly better matches the reference pattern of $Cu_4ZnGe_2Se_7$ when compared the $Cu_2CoGeSe_4$ reference pattern.

The heating profiles were then optimized to determine if any improvements could be made as maximum temperatures of 850 °C and 900 °C for 4 days were tested for all four potential new 4:1:2:7 compounds. After XRPD analysis, it was clear that all patterns provided many secondary phases with lots of impurity peaks, except for $Cu_4FeGe_2Se_7$. At the 850 °C heating profile for 4 days $Cu_4FeGe_2Se_7$ looked almost phase-pure, but as seen previously, it very closely matched the corresponding 2:1:1:4 reference pattern as well (Figure A.6). Again, closer examination of the XRPD pattern around 46° 2θ reveals that the experimental pattern better matches the 4:1:2:7 reference which suggests the discovery of a new compound (Figure A.7).

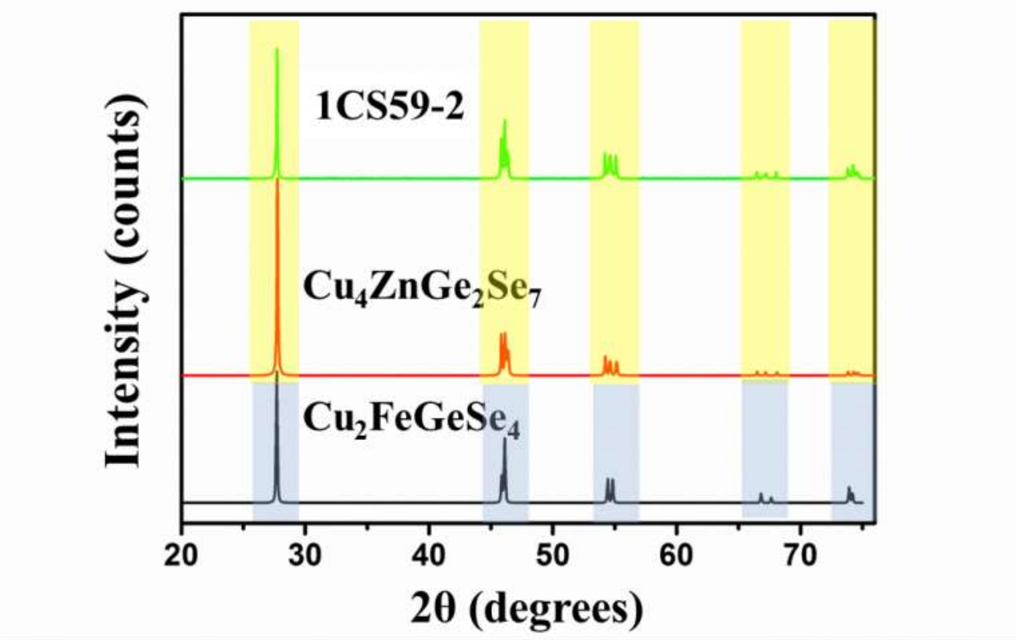

Figure A.6. XRPD pattern intended to prepare $Cu_4FeGe_2Se_7$ at 800 °C for 4 days which very closely matches the reference patterns of both $Cu_4ZnGe_2Se_7$ and $Cu_2FeGeSe_4$.

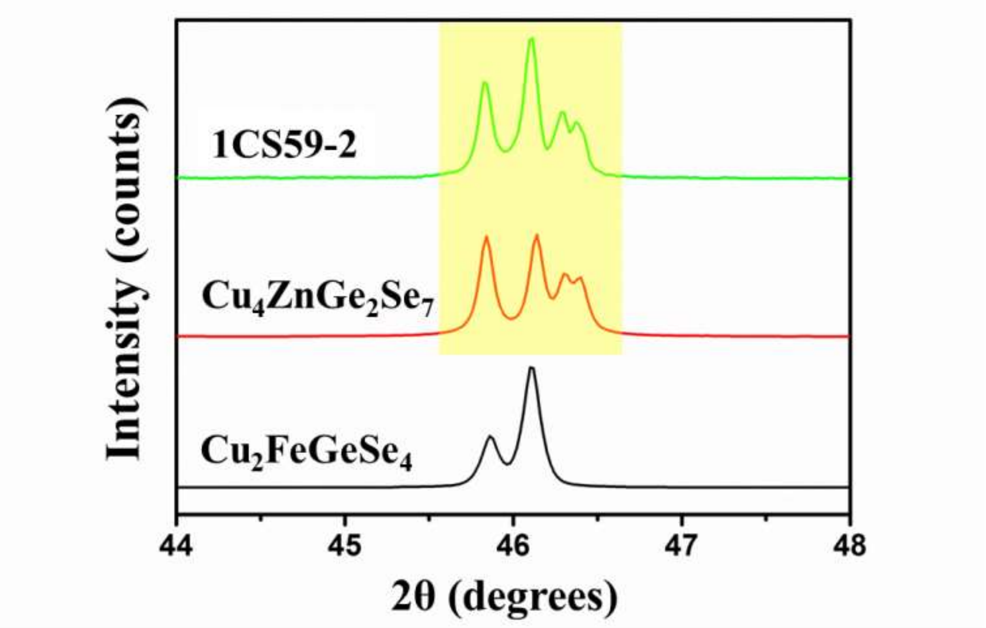

Figure A.7. Closer examination of the XRPD pattern intended to prepare $Cu_4FeGe_2Se_7$ at 800 °C for 4 days clearly better matches the reference pattern of $Cu_4ZnGe_2Se_7$ when compared the $Cu_2FeGeSe_4$ reference pattern.

In the pursuit of structural data for these new compounds, single crystal data was collected for both $Cu_4CoGe_2Se_7$ and $Cu_4FeGe_2Se_7$. Full integration of data could not be completed for multiple crystals tested of the $Cu_4CoGe_2Se_7$ compound. However, the structure was solved and refined for the $Cu_4FeGe_2Se_7$ compound. It is isostructural with $Cu_4ZnGe_2Se_7$, as they both have the *C*2 space group with atoms on the same crystallographic locations. The crystallographic data for $Cu_4FeGe_2Se_7$ is shown in Table A.1. Atomic coordinates, as well as bond lengths and angles are displayed in Tables A.2 and A.3, respectively.

Table A.1. Crystallographic data and experimental details for $Cu_4FeGe_2Se_7$.

Formula	$Cu_4FeGe_2Se_7$
Size (mm)	0.32 × 0.14 × 0.08
Temperature (K)	296(2)
Space group, No.	*C*2, 5
a (Å)	12.3442(4)
b (Å)	5.6076(2)
c (Å)	8.7675(3)
β (°)	98.633(2)
Volume (Å^3), Z	600.02(4), 2
Density (Mg/m^3)	5.579
Reflections collected/unique	5813/2152
Data/Restraints /Parameters	2152/1/67
Completeness to theta = 33.30°	94.8 %
Goodness of fit	1.096
Final R indices [$I > 2\sigma(I)$]	R1 = 0.0456, wR_2 = 0.1311
R indices (all data)	R1 = 0.0521, wR_2 = 0.1369
Highest peak, deepest hole (e/Å^3)	2.093, -1.931

Refinement of F^2 was made against all reflections.

$R_1 = (\Sigma||F_o|-|F_c||)/(\Sigma|F_o|)$,

$wR_2 = \sqrt{(\Sigma[w(F_o^2-F_c^2)^2]/\Sigma[w(F_o^2)^2])}$,

$w = 1/(\sigma^2(F_o^2) + (aF_o)^2 + bP)$, $P = [2F_c^2 + Max(F_o^2,0)]/3$

Table A.2. Atomic coordinates and isotropic displacement parameters (U_{iso}) obtained from single crystal data of $Cu_4FeGe_2Se_7$.

Site	**Multiplicity Wyckoff Letter**	**x**	**y**	**z**	**U_{iso} Å^2**
Cu1	4c	0.1426(1)	0.2455(3)	0.9312(1)	0.020(1)
Cu2	4c	0.2851(1)	0.2530(2)	0.3597(1)	0.011(1)
Fe1	2a	0.0000	0.2582(5)	0.5000	0.016(1)
Ge1	4c	0.4324(1)	0.2660(3)	0.7832(1)	0.012(1)
Se1	2b	0.0000	0.5136(2)	0.0000	0.014(1)
Se2	4c	0.2867(1)	0.4948(2)	0.8546(1)	0.007(1)
Se3	4c	0.0738(1)	0.0042(2)	0.7139(1)	0.013(1)
Se4	4c	0.3596(1)	0.0050(1)	0.5787(1)	0.008(1)

Table A.3. Bond distances (Å) and angles (°) from single crystal data of Cu$_4$FeGe$_2$Se$_7$.

Cu1—Se3i	2.387(2)	Se3i—Cu1—Se2	109.64(8)
Cu1—Se2	2.406(2)	Se3i—Cu1—Se3ii	106.98(4)
Cu1—Se3ii	2.387(1)	Se2—Cu1—Se3ii	110.90(3)
Cu1—Se1	2.457(1)	Se3i—Cu1—Se1	111.14(4)
		Se2—Cu1—Se1	110.84(4)
		Se3ii—Cu1—Se1	107.25(7)
Cu2—Se2	2.402(1)	Se2—Cu2—Se3	108.01(7)
Cu2—Se3	2.387(2)	Se2—Cu2—Se4	109.09(4)
Cu2—Se4	2.405(1)	Se3—Cu2—Se4	109.66(3)
Cu2—Se4iii	2.401(1)	Se2—Cu2—Se4iii	111.37(3)
		Se3—Cu2—Se4iii	110.06(3)
		Se4—Cu2—Se4iii	108.63(7)
Fe1—Se3iv	2.422(1)	Se3iv—Fe1—Se3	109.52(9)
Fe1—Se3	2.422(1)	Se3iv—Fe1—Se4v	110.97(2)
Fe1—Se4v	2.398(1)	Se3—Fe1—Se4v	108.71(2)
Fe1—Se4vi	2.398(1)	Se3iv—Fe1—Se4vi	108.71(2)
		Se3—Fe1—Se4vi	110.97(2)
		Se4v—Fe1—Se4vi	107.94(8)
Ge1—Se3	2.349(1)	Se3—Ge1—Se2vii	112.56(8)
Ge1—Se2vii	2.368(1)	Se3—Ge1—Se4viii	111.42(3)
Ge1—Se4viii	2.384(1)	Se2vii—Ge1—Se4viii	108.42(3)
Ge1—Se1ix	2.415(1)	Se3—Ge1—Se1ix	110.76(3)
		Se2vii—Ge1—Se1ix	107.21(3)
		Se4viii—Ge1—Se1ix	106.18(7)

Symmetry codes: (i) $-x+1/2, y-1/2, -z+1$; (ii) $x, y-1, z$; (iii) $-x+1/2, y+1/2, -z$; (iv) $-x, y, -z$; (v) $x-1/2, y-1/2, z$; (vi) $-x+1/2, y-1/2, -z$; (vii) $x+1/2, y+1/2, z$; (viii) $x, y+1, z$; (ix) $x+1/2, y+3/2, z$.

References

---

[1] H. Katagiri, K. Jimbo, S. Yamada, T. Kamimura, W. S. Maw, T. Fukano, T. Ito, T. Motohiro, *Appl. Phys. Expr.* **2008**, *1*, 041201-041202.

[2] R. A. Wibowo, E. S. Lee, B. Munir, K. H. Kim, *Phys. Status Solidi A* **2007**, *204*, 3373-3379.

[3] H. Matsushita, T. Ochiai, A. Katsui, *J. Cryst. Growth* **2005**, *275*, e995-e999.

[4] T. K. Todorov, K. B. Reuter, D. B. Mitzi, *Adv. Mater. (Weinheim, Ger.)* **2010**, *22*, E156-E159.

[5] D. Chen, N. M. Ravindra, *J. Alloys and Compounds* **2013**, *579*, 468-472.

[6] J. W. Lekse, M. A. Moreau, K. L. McNerny, J. Yeon, P. S. Halasyamani, J. A. Aitken, *Inorg. Chem. (Washington, DC, U. S.)* **2009**, *48*, 7516-7518.

[7] M. L. Liu, F. Q. Huang, L. D. Chen, I. W. Chen, *Appl. Phys. Lett.* **2009**, *94*, 202103-202105.

[8] C. Sevik, T. Cagin, *Phys. Rev. B* **2010**, *82*, 045202-045208.

[9] X. Y. Shi, F. Q. Huang, M. L. Liu, L. D. Chen, *Appl. Phys. Lett.* **2009**, *94*, 122103.

[10] C. Persson, *J. App. Phys.* **2010**, *107*, 053710.

[11] L. Choubrac, A. Lafond, C. Guillot-Deudon, Y. Moëlo, S. Jobic, *Inorg. Chem.* **2012**, *51(6)*, 3346-3348.

[12] C. B. Brunetta, W. C. Minsterman III, C. Lake, J. A. Aitken, *J. Solid State Chem.* **2012**, *187*, 177-185.

[13] B. C. Sales, D. Mandrus, R. K. Williams, *Science* **1996**, *272*, 1325-1328.

[14] G. S. Nolas, D. T. Morelli, T. M. Tritt, T. M. *Annu. Rev. Mater. Sci*. **1999**, *29*, 89-116.

[15] E. S. Toberer, A. F. May, G. J. Synder, *Chem. Mater.* **2010**, *22*, 624-634.

---

[16] J. Graff, S. Zhu, T. Holgate, J. Peng, J. He, T. M. Tritt, *J. Electron Mater.* **2011**, *40*, 696-701.

[17] A. Postnikov, N. B. Mortazavi Amiri, *Phys. Rev. B.* **2010**, *82*, 205204.

[18] L. J. A. Koster, V. D. Mihailetchi, and P. W. M. Blom, *Appl. Phys. Lett.* **2006**, *88*, 093511.

[19] C. Renouf, *Nat. Chem*. **2012**. *4,* 862-862.

[20] M.-L. Liu, I.-W. Chen, F.-Q. Huang, L.-D. Chen, *Adv. Mater.* **2009**, *21(37)*, 3808-3812.

[21] M. C. Ohmer, R. Pandey, *MRS Bull*. **1998**. *23(7)*, 16-22.

[22] G. C. Bhar, R. C. Smith, *Phys. Status Solids* **1972**, *13*, 157-168.

[23] J. A. Brant, D. J. Clark, Y. S. Kim, J. I. Jang, J. H. Zhang, J. A. Aitken, *Chem. Mater.* **2014**, *26*, 3045-3048.

[24] J. A. Brant, D. J. Clark, Y. S. Kim, J. I. Jang, A. Weiland, J. A. Aitken, *Inorg. Chem.* **2015**, *54*, 2809-2819.

[25] M.-L. Liu, I.-W. Chen, F.-Q. Huang, L.-D. Chen, *Appl. Phys. Lett*. **2009**, *94*, 202103.

[26] E. Parthé, Gordon and Breach Science Publishers, New York, NY, **1964**.

[27] J. C. Anderson Goryunova, (Eds.), The MIT Press, Cambridge, MA. **1965**.

[28] T. Goertzel, B. Goertzel, Basic Books: New York, **1996**.

[29] L. Pauling *J. Am. Chem. Soc*. **1929**, *51*, 1010–1026.

[30] C. D. Brunetta, J. A. Brant, K. A. Rosmus, K. M. Henline, E. Karey, J. H. MacNeil, J. A. Aitken, *J. Alloys and Compd.* **2013**, *574*, 495-503.

[31] B. Pamplin, *Prog. Cryst. Growth Charact.* **1981,** *3*, 179-192.

[32] R. Nitsche, D. F. Sargent, P. Wild, *J. Cryst. Growth* **1967**, *1*, 52-53.

---

[33] D. M. Schleich and A. Wold, *Mat. Res. Bull.* **1977**, *12*, 111.

[34] C. I. Lee and C. D. Kim, *J. Kor. Phys. Soc.* **2000**, *37*, 364-367.

[35] H. Matsushita, A. Katsui, *J. Phys. Chem. Sol.* **2005**, *66*, 1933-1936

[36] P. U. Bhaskar, G. S. Babu, Y. B. Kumar, V. S. Raja *Thin Solid Films* **2013**, *534*, 249-254.

[37] W. Schäfer and R. Nitsche, *Mater. Res. Bull.* **1974**, 9, 645.

[38] W. Schäfer , K. Scheunemann, R. Nitsche, *Mat. Res. Bull.* **1980**, *15*, 933-937.

[39] L. D. Gulay, I. D. Oleksuyuk, O. V. Parasyuk, *J. Alloys Compd.* **2002**, *340*, 157-166.

[40] S. C. Riha, B.A. Parkinson, A. L. Prieto, *J. Am. Chem. Soc.* **2009**, *131*, 12054-12055.

[41] N. Beigom, M. Amiri, A. Postnikov *Phys. Rev.* **2010**, *82*, 205204.

[42] C. Steinhagen, M. G. Panthani, V. Akhavan, B. Goodfellow, B. Koo, B.A. Korgel, *J. Am. Chem. Soc.* **2009**, *131*, 12554-12555.

[43] D. J. Xue, F. Jiao, H. J. Yan, X. Wei, D. Zhu, Y. G. Guo, *Chem. Asian J.* **2013**, *8*, 2383-2387.

[44] B. J. Stanbery, *Rev. Solid State Mater. Sci.*, **2002** *27(2)*, 73-117.

[45] M. Hamdi, A. Lafond, C. Guillot-Deudon, F. Hlel, M. Gargouri, S. Jobic, *J. Solid State Chem.* **2014**, *220*, 232-237.

[46] N. Nakayama, K. Ito, *Appl. Surf. Sci.* **1996**, *92*, 171-175.

[47] Q. Guo, H.W. Hillhouse, R. Agrawal, *J. Am. Chem. Soc.* **2009**, *13*, 11672-11673.

[48] H. Katagiri, K. Jimbo, W.S. Maw, K. Oishi, M. Yamazak, H. Araki, A. Takeuchi, *Thin Solid Films* **2009**, *517*, 2455-2460.

[49] P. A. Franken, A. E. Hill, C. W. Peters, G. Weinreich, *Phys. Rev. Lett.* **1961**, *4*, 118-119.

---

[50] S. Sasaki, Y. Mori, M. Yoshimura, Y. K. Yap, T. Kamimura, *Mater. Sci. Eng. R-Rep.* **2000**, *30*, 1-54.

[51] K. Wang, C. Fang, J. Zhang, X. Sun, S. Wang, Q. Gu, X. Zhao, B. J. Wang, *J. Cryst. Growth* **2006**, *287*, 478-482.

[52] P. G. Schunemann, *Proc. SPIE* **2007**, *6455*, 64550R.

[53] R. J. Clewes, C. R. Howle,; D. J. M. Stothard, M. H. Dunn, G. Robertson, W. Miller, G. Malcolm, G. Maker, R. Cox, B. Williams, M. Russell, *Proc. SPIE* **2012**, *8456*, 85460X.

[54] W. Lu, L. Liu, J. Sun, W. Pan, *Opik*, **2008**, *119*, 388–394.

[55] a) V. Vaicikauskas, M. Kaucikas, V. Swedas, Z. Kuprionis, *Rev. Sci. Instrum.* **2007**, *78*, 023106; b) Y. M. Andreev, P. P. Geiko, G. M. Krekov, O. A. Romanovskii, *Proc. SPIE* **1991**, *1811*, 367–370.

[56] C. F. Sun, C. L. Hu, X. Xu, B. P. Yang, J. G. Mao, *J. Am. Chem. Soc.* **2011**, *133*, 5561-5572.

[57] K. A. Rosmus, J. A. Brant, S. D. Wisneski, D. J. Clark, Y. S. Kim, J. I. Jang, C. D. Brunetta, J. H. Zhang, M. N. Srnec, J. A. Aitken, *Inorg. Chem.* **2014**, *53*, 7809-7811.

[58] H. Kildal, G. W. Iseler, *Appl. Opt.* **1976**, *15*, 3062-3065.

[59] J. W. Lekse, M. A. Moreau, K. L. McNerny, J. Yeon, P. S. Halasyamani, J. A. Aitken, *Inorg. Chem.* **2009**, *48*, 7516-7518.

[60] V. V. Atuchin, B. I. Kidyarov, N. V. Pervukhina, *Comput. Mater. Sci.* **2006**, *37*(4), 507-511.

[61] K. Wu, Chen, C. *Appl. Phys. A* **1992**, *54(3)*, 209-220.

---

[62] T. K. Bera, J. H. Song, A. J. Freeman, J. I. Jang, J. B. Ketterson, M. G. Kanatzidis, *Agnew. Chem. Int. Ed.* **2008**, *120*, 7946-7950.

[63] F. J. DiSalvo, *Science* **1999**, *285*, 703.

[64] G. Chen, M. S. Dresselhaus, G. Dresselhaus, J. P. Fleurial, T. Caillat, *Int. Mater. Rev.* **2003**, *48*, 45.

[65] J. C. Peltier, *Ann. Chem.* **1834**, *56*, 371-387.

[66] L. Bell, *Science* **2008**, *321*, 1457-1461.

[67] F. R. Stabler, *Mater. Res. Soc. Symp. Proc.* **2006**, *886*, # 0886-F01-04.1

[68] W. G. Zeier, Y. Pei, G. Pomrehn, T. Day, N. Heinz, C.P. Heinrich, G.J. Snyder, W. Tremel, *J. Am. Chem. Soc.* **2013**, *135*, 726-732.

[69] T. M. Tritt, M. A. Subramanian, *MRS Bull.* **2009**, *31*, 188-198.

[70] S. K. Bux, R. G. Blair, P. K. Gogna, H. Lee, G. Chen, M. S. Dresselahus, *Adv. Funct. Mater.* **2009**, *19*, 2445-2452.

[71] M. L. Lui, I. W. Chen, F. Q. Huang, L. D. Chen, *Adv. Mater.* **2009**, *21*, 3808-3812.

[72] C. X. Xiao, K. Li, J. Zhang, W. Tong, Y. Liu, Z. Li, P. Huang, B. Pan, H. Su, Y. Xie, *Mater. Horiz.* **2014**, *1*, 81.

[73] X. Lu, D. T. Morelli, *J. Electron. Mater.* **2012**, *41*, 1554-1558.

[74] S. K. Bux, J. P. Fleurial, R. B. Kaner, *Chem. Commun.* **2010**, *46*, 8311-8324.

[75] G. Tan, F. Shi, J. W. Doak, H. Sun, L.-D. Zhao, P. Wang, C. Uher, C. Wolverton, V. P. Dravid and M. G. Kanatzidis, *Energy Environ. Sci.* **2015, *8*,** 267-277.

[76] W. G. Zeier, A. LaLonde, Z. M. Gibbs, C. P. Heinrich, M. Panthofer, G. J. Snyder, W. Tremel, *J. Am. Chem. Soc.* **2012**, *134*, 7147-7154.

---

[77] M. Ibanex, R. Zamani, A. LaLonde, D. Cadavid, W. Li, A. Shavel, J. Arbiol, J. R. Morante, S. Gorsse, G. J. Snyder, A. Cabot, *J. Am. Chem. Soc.* **2012**, *134*, 4060-4063.

[78] W. Tremel, W. G. Zeier, A. LaLonde, Z. M. Gibbs, C. P. Heinrich, M. Panthofer, G. J. Snyder, *J. Am. Chem. Soc.* **2012**, *134*, 7147-7154.

[79] Bruker **1998** SMART and SAINT, Bruker AXS Inc., Madison, Wisconsin, USA.

[80] G. M. Sheldrick, **2002** SADABS. University of Göttingen, Germany.

[81] G. M. Sheldrick, *SHELXTL, Crystallographic Software Package*, Version 5.1; Bruker-AXS: Madison, WI, **1998**.

[82] X.p.H. Plus, PANalytical B.V., Almelo, the Netherlands.

[83] J. Wang, B. H. Toby, P. L. Lee, L. Ribaud, S. Antao, C. Kurtz, M. Ramanathan, R. B. Von Dreele, M. A. Beno, *Rev. Sci. Instrum.* **2008**, *79*, 085105-085111.

[84] P. L. Lee, D. Shu, M. Ramanathan, C. Preissner, J. Wang, M. A. Beno, R. B. Von Dreele, L. Ribaud, C. Kurtz, S. M. Antao, X. Jiao, B. H. Toby, *J. Synchrotron Radiat.* **2008**, *15*, 427-432.

[85] B. H. Toby, *J. Appl. Crystallogr.* **2001**, *34*, 210-213.

[86] L. R. Dalesio, J. O. Hill, M. Kraimer, S. Lewis, D. Murray, S. Hunt, W. Watson, M. Clausen, J. Dalesio, *Nucl. Instrum. Methods Phys. Res., Sect. A.* **1994**, *352*, 197-184.

[87] A. C. Larson, R. B. Von Dreele, *Los Alamos National Laboratory Report LAUR* **1994**, 86-748.

[88] O. V. Parasyuk, L. D. Gulay, Y. E. Romanyuk, L. V. Piskach, *J. Alloys Compd.* **2001**, *329*, 202-207.

[89] M. Abramowitz, I. A. Stegun, (Eds.), Handbook of Mathematical Functions, Dover Publications, Dover, NY, **1965**. (Ch. 22).

---

[90] P. Kubelka, F. Monk, *Z. Technol. Phys.* **1931**, *12*, 593–601.

[91] F. Urbach, *Phys. Rev.* **1953**, *92*, 1324.

[92] R. J. McGowan, *Anal. Chem.* **1963,** *35*, 1664-1665.

[93] M. D. Segall, P. J. D. Lindan, M. J. Probert, C. J. Pickard, P. J. Hasnip, S. J. Clark, M. C. Payne, *J. Phys.: Condens. Matter* **2002**, *14*, 2717-2744.

[94] V. Milman, B. Winkler, J. A. White, C. J. Pickard, M. C. Payne, E. V. Akhmatskaya, R. H. Nobes, *Int. J. Quantum Chem.* **2000**, *77*, 895-910.

[95] W. Kohn, L. Sham, *Phys. Rev. A* **1965**, *140*, 1133-1138.

[96] J. S. Lin, A. Qteish, M. C. Payne, V. Heine, *Phys. Rev. B* **1993**, *47*, 4174-4180.

[97] R. S. Mulliken, *J. Chem. Phys.* **1955**, *23*, 1833–1840.

[98] M. D. Segall, R. Shah, C. J. Pickard, M. C. Payne, *Phys. Rev. B* **1996**, *54*, 16317-16320.

[99] G. A. Slack, *CRC Handbook of Thermoelectrics*. **1995**, CRC Press, Boca Raton, FL. 407-409.

[100] E. Parthe, J. Garin, *Monatsh. Chem.* **1971**, *102*, 1197.

[101] C. Yeh, Z.W. Lu, S. Froyen, A. Zunger, *Phys. Rev. B: Condens. Matter* **1992**, *46*, 10086.

[102] P. D. Lao, Y. Guo, G. G. Siu, S. C. Shen, *Phys. Rev. B: Condens. Matter* **1993**, *48*, 11701.

[103] H. Matsushita, T. Maeda, A. Katsui, T. Takizawa, *J. Cryst. Growth* **2000,** *208*, 416.

[104] J. I. Pankove, *Optical Processes in Semiconductors*, Dover Publication, New York, **1971**, 412-413.

[105] B. Choudhury, M. Dey, A. Choudhury, *Int. Nano Lett.* **2013**, *3*, 25.

---

[106] A. C. Malingowski, P. W. Stephens, A. Huq, Q. Huang, S. Khalid, P. G. Khalifah, *Inorg. Chem.* **2012**, *51*, 6096-6103.

[107] N. W. Ashcroft, N. D. Mermin, *Solid State Phys.*, Harcourt Brace and Company, Orlando **1976**, 652.

[108] J. Tauc, *MRS Bull*. **1968**, *3*, 37– 46.